

# Replacement-Type Quantum Gates

Florian Ginzel,<sup>1</sup> Javad Kazemi,<sup>1</sup> Valentin Torgler,<sup>1</sup> and Wolfgang Lechner<sup>1, 2, 3, 4</sup>

<sup>1</sup>*Parity Quantum Computing Germany GmbH, Schauenburgerstraße 6, 20095 Hamburg, Germany*

<sup>2</sup>*Parity Quantum Computing GmbH, Rennweg 1, Top 314, 6020 Innsbruck, Austria*

<sup>3</sup>*Parity Quantum Computing France SAS, 10 Avenue de Kleber, 75016 Paris, France*

<sup>4</sup>*Institute for Theoretical Physics, University of Innsbruck, 6020 Innsbruck, Austria*

(Dated: August 4, 2025)

We introduce the paradigm of replacement-type quantum gates. This type of gate introduces input qubits, candidate qubits, and output qubits. The candidate qubits are prepared such, that a displacement conditional on the input qubit results in the targeted output state. Finally, the circuit continues with the output qubits constructed from the candidate qubits instead of the input qubits, thus the name "replacement-type gate". We present examples of replacement-type  $X$  and CNOT gates realized with spin qubits and with neutral atom qubits. By making use of the extended Hilbert space, including the position of the particles, these gates approximately preserve the innate noise bias of the qubits. The gate preserves the noise-bias which motivates advanced quantum computer architectures with error correction.

## I. INTRODUCTION

Quantum computing platforms are at the cusp of advancing beyond laboratory-scale proof-of-principle demonstrations. However, all types of qubits are vulnerable to environmental noise and are therefore error-prone, making quantum error correction (QEC) a necessity before real-world problems can be tackled [1–3]. A large number of generic QEC codes have been proposed, however, the overhead required for successful error correction is widely considered prohibitive for large-scale applications on near-term hardware [4–9].

One strategy for alleviating the requirements for QEC is to rely on specific advantages of the underlying hardware, which is oftentimes described by a less destructive error model than assumed for a general-purpose QEC code [10–13]. Particularly beneficial are biased-noise qubits, where one type of error – phase errors, modelled by the  $\sigma_z$  Pauli matrix, or bit errors, modelled by  $\sigma_x$  – is dominant. A strong noise bias allows for asymmetric quantum or even classical codes for error correction [11–19].

An innate noise bias is found in many physical systems, for example semiconductor spin qubits, where the qubit is formed by the spin-1/2 of an electron or hole confined to an effectively zero-dimensional quantum dot (QD) by an engineered electrostatic potential [20, 21]: Here, the noise is dominated by electrical fluctuations which rarely flip the spin but contribute to dephasing [22–25]. Another prominent example is neutral atom qubits, where the electronic states of Rydberg atoms trapped in optical potentials encode quantum information [26, 27]. In this case, a highly excited valence electron originating from a certain qubit state mediates strong interaction with nearby atoms, which is then used to engineer entangling gates. Such gates are highly biased towards phase errors since only one of the qubit states is involved in the gate operation under careful engineering of the qubit encoding [18].

The noise bias of these qubit types is not necessarily

preserved by gate operations for quantum computing. A phase (bit) error occurring during a rotation of a qubit on the Bloch sphere is partially or entirely translated into a bit (phase) error, resulting in a depolarizing rather than a biased noise. Furthermore, a common decomposition of the  $\text{CNOT}_{q_c, q_t}$  gate is  $H_{q_t} \text{CZ}_{q_c, q_t} H_{q_t}$  since CZ is a native gate to many platforms [28–34]. Here, the Hadamard gates  $H_{q_t}$  temporarily swap the  $z$ - and  $x$ -bases on the target qubit  $q_t$ , effectively inverting the noise bias on  $q_t$  for the duration of the gate. However, the benefit for QEC is maximal if the noise bias is preserved throughout all operations in a quantum circuit.

A noise-bias-preserving gate set with this property is known for bosonic cat qubits [14, 15, 35, 36] but remains elusive in general. In fact, a no-go theorem states that a noise-bias-preserving CNOT gate is impossible in a system with finite Hilbert space [14]. Nonetheless, approximately biased-noise gates can be designed if the quantum state is not confined to the Bloch sphere of the qubit's Hilbert space, avoiding the problematic rotations. One example is known for Rydberg atoms, harnessing additional hyperfine states of the atoms [18].

A larger Hilbert space does not necessarily require additional internal states of the qubit. In several quantum computing platforms, the qubits are formed in the internal degrees of freedom of indistinguishable particles confined by an engineered potential, e.g., electrons or holes in QDs and trapped atoms or ions [33]. These particles can be shuttled – physically moved to remote sites by displacing the potential minimum of a qubit. Shutting has gained much attention as a method for mediating interactions between distant qubits and for moving qubits to dedicated readout, manipulation or interaction zones [34, 37–46].

In this paper, we propose a new paradigm for single- and two-qubit quantum gates which entirely avoid rotations of the qubit on the Bloch sphere. By hybridizing the qubit state with the positional degree of freedom of the particle the Hilbert space is extended beyond the Bloch sphere, allowing an approximately noise-bias-preserving

gate. Key element of the gate is a quantum operation which replaces the original qubit with a candidate qubit, conditional on the input state. We present the general framework and discuss possible realizations for both QD spin qubits and Rydberg atom qubits. In both cases our investigation of the error mechanisms shows that the gates can indeed be approximately noise-bias-preserving, and we identify the leading error sources.

This paper is organized as follows. We introduce the general concept of replacement-type gates in Sec. II. Subsequently, in Sec. III A, we introduce the required primitives for spin-1/2 qubits in semiconductor QDs, in Sec. III B we present concrete examples of replacement-type gates, in Sec. III C we discuss the impact of various error mechanisms on the gates and the noise bias, and in Sec. III D we estimate the performance. Analogously, a realization with neutral atom qubits is presented in Sec. IV. In Sec. V, we summarize our findings and give an outlook.

## II. REPLACEMENT-TYPE GATES

Here, we present the abstract concept underlying our proposed replacement-type quantum gate. The core idea is to directly exploit the positional degree of freedom of a mobile qubit to implement a quantum gate, following the protocol outlined below. We consider a register comprised of multiple sites, where the position of a qubit and the the occupation number of a site are quantum mechanical observables.

To implement a quantum operation  $U$  on one or multiple input qubits as replacement-type gate, auxiliary qubits need to be initialized in the states  $U|\psi_i\rangle$ , where the set of all  $|\psi_i\rangle$  forms a basis of the Hilbert space  $U$  is acting upon. We refer to these auxiliary qubits as the candidate qubits, they are designated to replace the input qubits at the end of the gate. This is achieved through a suitable rearrangement operation, which coherently moves one candidate qubit per input qubit to a designated output site, conditional on the state of the input qubits. The entangled state of input and candidate qubits created by the rearrangement operation can then be disentangled by an appropriate disentangling operation, which discards all qubits except the population of the output site. The remaining output qubits are kept instead of the input qubits. The procedure is illustrated in Fig. 1.

First, we consider a single input qubit in the state  $|\psi_{\text{in}}\rangle = \alpha_0|0\rangle + \alpha_1|1\rangle$ , to which a quantum gate  $U$  should be applied. The basis states are transformed by  $U$  as  $U|0(1)\rangle = |0_U(1_U)\rangle$  and we assume that it is possible to directly initialize qubits in both states  $|0_U\rangle$  and  $|1_U\rangle$ . This may not be possible for arbitrary states, such that only discrete gates are allowed.

In the first step of the replacement-type gate, we introduce a register with three sites occupied by two candidate qubits in the state  $|0_U, 1_U, x\rangle$ , where  $x$  indicates

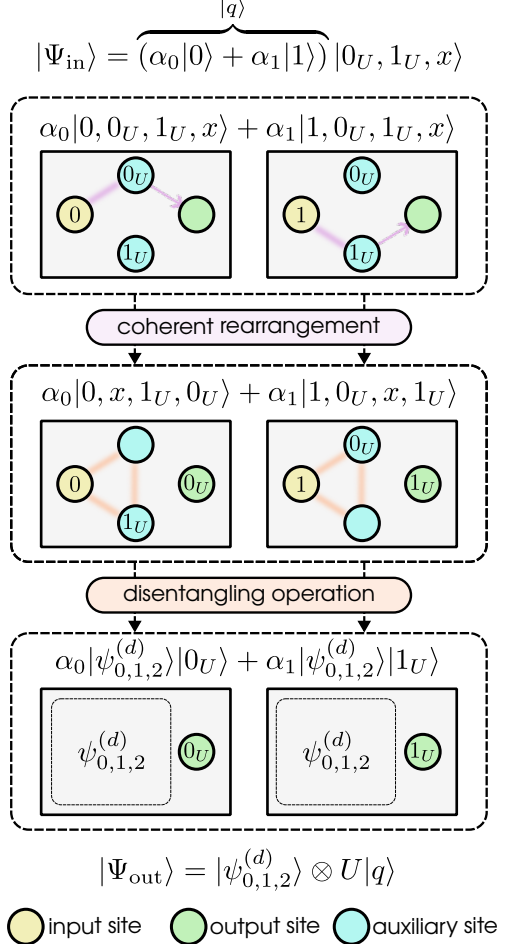


FIG. 1. Concept of the replacement-type single-qubit gate  $U$ . An input qubit has the general qubit state  $|q\rangle = \alpha_0|0\rangle + \alpha_1|1\rangle$  and is placed at the yellow input site. Two candidate qubits are initialized in suitable basis states of the Hilbert space  $U$ , here in the states  $|0_U(1_U)\rangle = U|0(1)\rangle$ , and are placed at the blue auxiliary sites, the green output site is initially empty,  $|x\rangle$ . Then, the register is rearranged coherently in order to transfer one of the candidate qubits into the output site, conditional on the state of the input qubit. This leads to an entangled state of all four qubits and the configuration of the positions. The amplitude  $\alpha_0$  ( $\alpha_1$ ) is now associated with state  $|0_U\rangle$  ( $|1_U\rangle$ ) at the output site, imposing the effect of the gate  $U$ . Disentangling the population of the output site from the rest of the register with suitable measurements leaves a single qubit in the final separable state  $|\psi_{0,1,2}^{(d)}\rangle \otimes U|q\rangle$ , corresponding to a gate  $U$  and a relocation of the qubit state.

an empty site. The empty site serves as the output site, which will eventually be populated with a qubit in the targeted state  $U|\psi_{\text{in}}\rangle$ . Note that we chose the output site to be an additional site for clarity here, a suitable rearrangement operation could also be configured such that one of the initially populated sites is chosen as output site. The total initial state is

$$|\Psi_{\text{in}}\rangle = (\alpha_0|0\rangle + \alpha_1|1\rangle)|0_U, 1_U, x\rangle. \quad (1)$$

In the next step, the qubits are rearranged by a unitary operation that maps

$$|0\rangle|0_U, 1_U, x\rangle \rightarrow |0\rangle|x, 1_U, 0_U\rangle, \quad (2)$$

$$|1\rangle|0_U, 1_U, x\rangle \rightarrow |1\rangle|0_U, x, 1_U\rangle. \quad (3)$$

The total state is thus transformed into an intermediate, entangled state

$$|\Psi_{\text{mid}}\rangle = \alpha_0|0\rangle|x, 1_U, 0_U\rangle + \alpha_1|1\rangle|0_U, x, 1_U\rangle. \quad (4)$$

The nature of this operation and the relevant interactions depend on the hardware platform and may not be possible for arbitrary  $U$ .

Following the rearrangement operation, the state of the qubit is encoded in a multi-particle state, Eq. (4), where the probability distribution for a measurement of the qubit state at the output site corresponds to a single qubit in the state  $U|\psi_{\text{in}}\rangle$ . However, if the qubit is not immediately measured following the gate, it is beneficial to disentangle the qubits again, since a hybrid state of multiple qubits and their position may be more vulnerable to environmental noise than the state of a single qubit.

Such a disentangling operation can be achieved through measurements performed in an appropriate basis. Introducing the superposition states  $|\pm\rangle = (|0\rangle \pm |1\rangle)/\sqrt{2}$ , the total state can be written as

$$|\Psi_{\text{mid}}\rangle = \frac{1}{\sqrt{2}}|+\rangle(\alpha_0|x, 1_U, 0_U\rangle + \alpha_1|0_U, x, 1_U\rangle) + \frac{1}{\sqrt{2}}|-\rangle(\alpha_0|x, 1_U, 0_U\rangle - \alpha_1|0_U, x, 1_U\rangle). \quad (5)$$

Measuring the state of the original input qubit in the basis  $\{|+\rangle, |-\rangle\}$ , results in the post-measurement state

$$\frac{1}{\sqrt{2}}(|0\rangle + s|1\rangle)(\alpha_0|x, 1_U, 0_U\rangle + s\alpha_1|0_U, x, 1_U\rangle), \quad (6)$$

where the relative phase  $s = (-1)^m$  is conditional on the measurement outcome  $m$ . Proceeding analogously with a measurement of the hybrid states  $(|x, 1_U\rangle \pm |0_U, x\rangle)/\sqrt{2}$  at the initial positions of the candidate qubits results in a separable state. We omit all qubits except the one remaining in the output site, which has the final state

$$|\psi_{\text{out}}\rangle = \alpha_0|0_U\rangle \pm \alpha_1|1_U\rangle = UZ^c|\psi_{\text{in}}\rangle, \quad (7)$$

with  $Z = |0\rangle\langle 0| - |1\rangle\langle 1|$ . Here,  $c$  is a classical bit obtained from the two measurement outcomes. Note that performing two separate measurements is not always necessary; if experimental constraints permit, a single measurement can be advantageous in mitigating measurement errors.

The final state is the targeted state  $U|\psi_{\text{in}}\rangle$  up to a phase flip that can be tracked by storing the measurement outcomes. Note that the disentangling operation does not require interaction between the auxiliary qubits and the output qubit, allowing the output qubit to be shuttled to a new location during the measurement. A

concrete example for a disentangling operation is discussed in Sec III B 2.

The generalization to multi-qubit gates is straightforward. For an operation  $U$  targeting  $N$  qubits, the rearrangement operations need to produce  $2^N$  configurations of the candidate qubits, corresponding to the action of  $U$  on a suitable basis of the multi-qubit Hilbert space. The main challenge of implementing the replacement-type gate lies in designing a feasible rearrangement operation. In the following chapters, we discuss examples based on two different hardware platforms.

We note that any errors occurring during the disentangling operation result in dephasing of the output qubit, regardless of the protocol: The objective of the disentangling operation is to transform a highly entangled state into a separable state,

$$|\Psi_{\text{mid}}\rangle = \alpha_0|\psi_{0,1,2}^{(0)}\rangle|0_U\rangle + \alpha_1|\psi_{0,1,2}^{(1)}\rangle|1_U\rangle \rightarrow |\Psi_{\text{out}}\rangle = |\psi_{0,1,2}^{(d)}\rangle(\alpha_0|0_U\rangle + \alpha_1|1_U\rangle), \quad (8)$$

where  $|\psi_{0,1,2}^{(0/1)}\rangle$  is the state of sites 0, 1 and 2 after the rearrangement operation, labelling them from left to right, and  $|\psi_{0,1,2}^{(d)}\rangle$  is their state after perfect disentangling. An error with probability  $p_d$  will result in the density matrix

$$\rho_{\text{out}} = (1 - p_d)|\psi_{0,1,2}^{(d)}\rangle(\alpha_0|0_U\rangle + \alpha_1|1_U\rangle)(\text{h.c.}) + p_d\left(\alpha_0|e_{0,1,2}^{(0)}\rangle|0_U\rangle + \alpha_1|e_{0,1,2}^{(1)}\rangle|1_U\rangle\right)(\text{h.c.}), \quad (9)$$

with the erroneous states  $|e_{0,1,2}^{(0/1)}\rangle$ , h.c. denotes the hermitian conjugate.

The subsequent discarding or resetting of the auxiliary qubits can be modelled as relaxation to the vacuum or ground state in these sites with unit probability. This leaves the output qubit dephased with probability  $p_d$ :

$$\rho_{\text{out}} \rightarrow (1 - p_d)(\alpha_0|0_U\rangle + \alpha_1|1_U\rangle)(\alpha_0^*|0_U| + \alpha_1^*|1_U|) + p_d(|\alpha_0|^2|0_U\rangle\langle 0_U| + |\alpha_1|^2|1_U\rangle\langle 1_U|). \quad (10)$$

Similarly, measurement errors will result in the wrong phase correction being applied to the output qubit. The observation that during the disentangling operation bit errors are translated into phase errors but not vice versa is an important result for considering the noise bias of the total gate.

### III. REALIZATION WITH SPIN QUBITS

In this section, we consider qubits encoded in the spins of confined electrons [47]. The confinement is achieved by creating a two-dimensional electron gas at the interface of a semiconductor heterostructure, such that the conduction band offset provides out-of-plane confinement. In-plane confinement is then achieved by electrostatic gating [21]. A sketch of such QDs is depicted in Fig. 2.

We consider an array of  $N$  QDs where only the orbital ground state is available in the few-electron regime. For

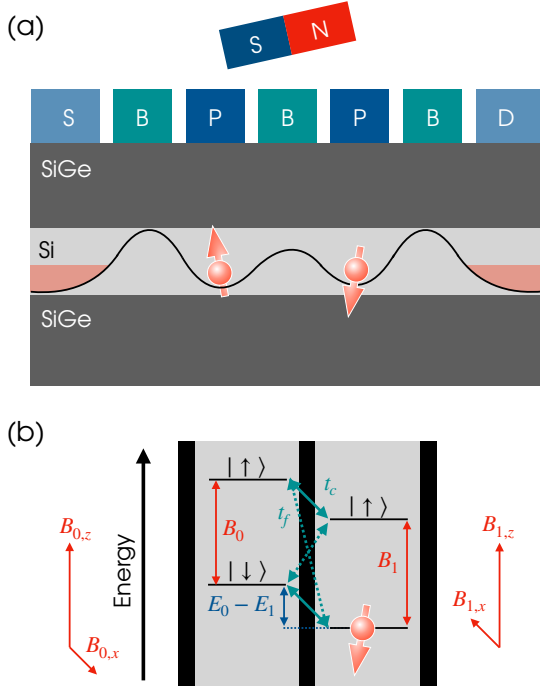


FIG. 2. (a) Sketch of two QDs in a Si/SiGe heterostructure. The electrical potential applied to plunger (P) and barrier (B) gates defines potential wells, which can be filled with single electrons or holes by coupling them to source (S) and drain (D) reservoirs. A strong magnetic field inhomogeneity, also referred to as synthetic spin-orbit interaction (SOI), is commonly created by a micromagnet. (b) Energy levels of two QDs, left (0) and right (1) occupied by a single spin. In each QD, two spin states  $|\downarrow\rangle$  and  $|\uparrow\rangle$  are available, with a splitting corresponding to the total magnetic field  $B_{0(1)}$  (red). A transverse magnetic gradient  $B_{0,x} - B_{1,x} \neq 0$  leads to non-collinear quantization axes. The energy detuning between the ground states,  $E_0 - E_1$  (blue), is set by the electrical potentials applied to the plunger gates. The voltage applied to the barrier gates tunes the tunneling between the QDs (teal) with a spin-conserving ( $t_c$ ) and spin-flipping ( $t_f$ ) matrix element.

simplicity, we neglect the valley degree of freedom, assuming a large valley splitting or a material where the conduction band minimum is non-degenerate [20, 48]. The system can be modelled with an extended Hubbard Hamiltonian [20],

$$\begin{aligned}
H_{\text{spin}} = & \sum_j^N \left( E_j n_j + \mathbf{B}_j \cdot \boldsymbol{\sigma}_j + \frac{U_2}{2} n_j (n_j - 1) \right) \\
& + \sum_j^{N-1} \sum_{\sigma, \sigma'} \left( t_{j, \sigma, \sigma'} (c_j^\sigma)^\dagger c_{j+1}^{\sigma'} + \text{h.c.} \right) \\
& + \sum_j^{N-1} U_1 n_j n_{j+1}. \tag{11}
\end{aligned}$$

Here,  $(c_j^\sigma)^\dagger$  annihilates (creates) an electron with spin

$\sigma$  in QD  $j$ ,  $n_j = \sum_\sigma (c_j^\sigma)^\dagger c_j^\sigma$  is the occupation number operator, and  $\boldsymbol{\sigma}_j$  is the vector of Pauli operators in QD  $j$ . The first line of Eq. (11) includes the electric on-site potential  $E_j$ , the magnetic field  $\mathbf{B}_j$  (given in energy units) in QD  $j$ , and the Coulomb repulsion  $U_2$  between two electrons in the same QD. An inhomogeneity  $\mathbf{B}_i \neq \mathbf{B}_j$  may arise from synthetic or intrinsic spin-orbit interaction (SOI). The second line of Eq. (11) describes the spin-conserving and spin-flipping tunneling between QDs  $j$  and  $j+1$  with matrix element  $t_{j, \sigma, \sigma'}$ , where h.c. denotes the Hermitian conjugate. The last line finally adds the Coulomb repulsion between the charges in neighboring QDs. Among these parameters,  $E_j$  and  $t_{j, \sigma, \sigma'}$  are electrically tunable during the experiment. The eigenstates of  $H_{\text{spin}}$  in the example  $N = 2$  with up to two electrons are illustrated in Fig. 3.

In the following, we discuss the physical mechanisms leveraged by the replacement-type gate in Sec. III A, then we present a realization of  $X$  and CNOT gates in Sec. III B. Finally, in Sec. III C, we discuss the dominant error mechanisms and in Sec. III D we simulate quantum process tomography to investigate the noise bias and to estimate the performance of the gates.

### A. Required Operations

With Loss-DiVincenzo qubits [47], defined by the spin of a single electron, the rearrangement operation can be constructed from well-known primitives. Typically, single-spin rotations in QD  $j$  are implemented by effectively realizing an oscillating magnetic field by periodically displacing the electron in an inhomogeneous magnetic field, known as electric dipole spin resonance (EDSR) [49, 50] or by electron spin resonance (ESR) with an oscillating transverse magnetic field  $B_{j,x}(t)$  [51]. The kinetic exchange is harnessed for coupling spins in adjacent QDs [52], depending on the longitudinal magnetic gradient this is an Ising- or Heisenberg-type interaction [20].

The replacement-type gate discussed in the following section represents a paradigm shift by leveraging different physical mechanisms. A key element is the conversion of a single-electron spin state into a charge state using Pauli spin blockade (PSB) [21, 52, 53]. Considering two QDs occupied by one electron each, the spin states form a singlet state  $|S_{(1,1)}\rangle = \frac{1}{\sqrt{2}} [(c_0^\uparrow)^\dagger (c_1^\downarrow)^\dagger - (c_0^\downarrow)^\dagger (c_1^\uparrow)^\dagger] |x\rangle$  and the three triplet states  $|T_0\rangle = \frac{1}{\sqrt{2}} [(c_0^\uparrow)^\dagger (c_1^\downarrow)^\dagger + (c_0^\downarrow)^\dagger (c_1^\uparrow)^\dagger] |x\rangle$  and  $|T_{\pm}\rangle = (c_0^{\uparrow(\downarrow)})^\dagger (c_1^{\downarrow(\uparrow)})^\dagger |x\rangle$ , where  $|x\rangle$  denotes an empty QD. Due to the Pauli principle, only the singlet state is allowed when both electrons occupy the same QD,  $|S_j\rangle = (c_j^\uparrow)^\dagger (c_j^\downarrow)^\dagger |x\rangle$ . Therefore, the triplet states are coupled to the states with double-occupation only via the typically weak spin-flip tunneling.

In the presence of a longitudinal magnetic field gradi-

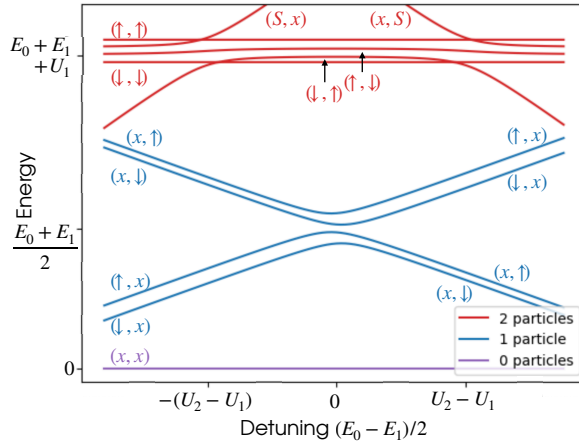


FIG. 3. Spectrum of a double QD in an inhomogeneous magnetic field occupied with no (purple), one (blue) or two (red) electrons as a function of the energy detuning. We label the states as  $(\sigma_0, \sigma_1)$  with the spin projection  $\sigma_{0(1)}$  in QD 0(1),  $x$  indicates an empty QD. With a single electron, avoided level crossings (ALCs) are opened at zero detuning by the tunneling matrix elements, far from the ALCs spin and position of the electron are good quantum numbers. The asymmetry is due to the longitudinal magnetic gradient. Adding a second particle leads to an offset in energy due to Coulomb repulsion, the two electrons can occupy a single QD only if their spins form a singlet ( $S$ ). Due to the longitudinal magnetic field gradient the singlet and triplet states decompose into the product states in the regime with one electron per QD.

ent  $B_{0,z} \neq B_{1,z}$ , the states  $|S_{(1,1)}\rangle$  and  $|T_0\rangle$  are no eigenstates anymore and rearrange themselves into the product states  $(c_0^\dagger)^{\dagger}(c_1^\dagger)^{\dagger}|x\rangle$  and  $(c_0^\dagger)^{\dagger}(c_1^\dagger)^{\dagger}|x\rangle$ , one of which is coupled to the  $|S_j\rangle$  singlet while the other one remains decoupled, as depicted in Fig. 3 [20, 21]. Throughout this section we assume a gradient such that  $(c_0^\dagger)^{\dagger}(c_1^\dagger)^{\dagger}|x\rangle$  is coupled to  $|S_0\rangle$

The inverse process of PSB, splitting a  $|S_j\rangle$  singlet into two QDs in the presence of a longitudinal magnetic field gradient, allows for the preparation of a product state of two spins. This technique is commonly used for spin qubit initialization. The  $|S_j\rangle$  singlet can be prepared by filling the QD with two electrons from a reservoir.

Spin-to-charge conversion can in principle also be achieved with a single electron, by precisely driving Landau-Zener transitions which emerge due to the SOI [54]. However, since this option is expected to be challenging in practice, we do not consider it further.

We further require the use of different shuttling techniques for manipulating the charge distribution [55]: Conveyor mode shuttling where the electrostatic potential  $E_j(t)$  at all sites is manipulated such that the entire potential landscape is uniformly displaced [37, 39], and bucket brigade shuttling. In bucket brigade shuttling, the detuning between two neighboring QDs,  $E_j(t) - E_{j+1}(t)$ , is swept through the avoided level crossing (ALC) such that a single electron tunnels from one QD to the next, which allows coherent spin transfer over short dis-

tances [54, 56]. In Fig. 3, bucket brigade shuttling corresponds to an adiabatic sweep through the ALCs of the blue single-particle states.

It has been shown that the Coulomb repulsion between neighboring QDs,  $U_1$ , can facilitate the displacement of a spin qubit conditional on the charge distribution of its surroundings [57]. Here, we envision an energy-selective bucket brigade tunneling, where the detuning  $\varepsilon(t) = E_j(t) - E_{j+1}(t)$  between QDs  $j$  and  $j+1$  is swept through the ALCs in the single-electron regime such that tunneling occurs if the target QD is empty but no tunneling occurs if the target QD is occupied. As can be seen in Fig. 3, this form of energy-selective tunneling is realistic if  $U_2 - U_1$  is sufficiently large compared to the tunneling matrix elements and the ALCs with one and two particles are well separated along the detuning axis. For a high-fidelity charge transition, the detuning at the final time  $t_f$  must be sufficiently far from the single-particle ALC,  $|\varepsilon(t_f)| \gg 2|t_{1,\sigma,\sigma}|$ , furthermore, for the charging energy to suppress movement in the case of two electrons the final detuning must be  $|\varepsilon(t_f)| \ll U_2 - U_1$ .

Finally, a measurement of the charge distribution will be required for the disentangling operation. A rapid and accurate measurement of the total occupation of a single QD is routinely obtained by means of a radio-frequency single electron transistor in the vicinity [23, 58–60]. Another method for detecting changes in the charge occupation is dispersive gate sensing, where the reflection of a microwave off one of the voltage gates of the QDs directly is monitored [61]. We emphasize that during the replacement-type gate no charge sensing must occur, otherwise the unintended (non-selective) measurement will lead to gate errors.

## B. Implementations of Replacement-Type Gates

In this section we present concrete examples of replacement-type gates: The rearrangement operation for an  $X$ -gate in Sec. III B 1, a related disentangling operation in Sec. III B 2, and a CNOT gate in Sec. III B 3.

### 1. Single-Qubit $X$ Gate

The design of the single-qubit gate follows the principles outlined in Sec. II and the protocol is illustrated in Fig. 4. A linear array of four QDs labeled 0 to 3 is required, where a specific arrangement of input and candidate qubits is prepared, using shuttling. We place the input qubit  $q$  in QD 1 and the two candidate qubits are placed in QDs 2 and 3 in the states  $|\uparrow_2\rangle$  and  $|\downarrow_3\rangle$ . Furthermore, a reference spin  $|\downarrow_0\rangle$  in QD 0 is required for PSB.

In the first step, spin-to-charge conversion via PSB is performed on QDs 0 and 1, such that the reference spin and the input qubit form a singlet state  $|S_0\rangle$  in QD 0 if

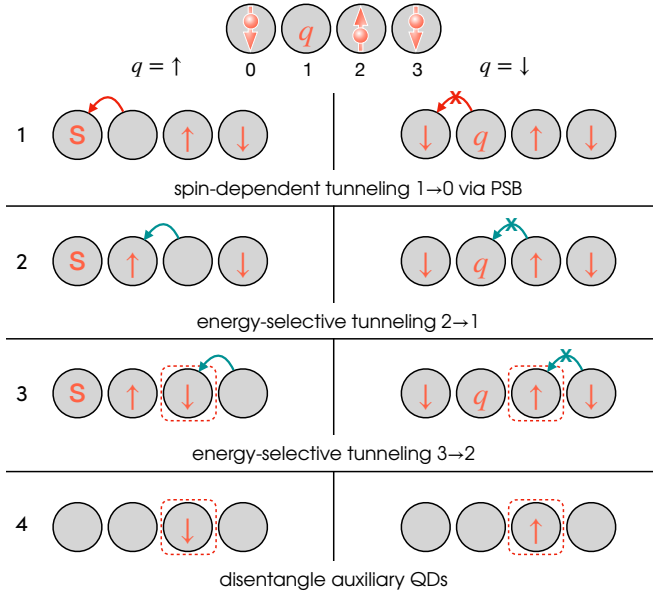


FIG. 4. Protocol for a replacement-type  $X$  gate with spin qubits. The initial configuration of the array of four QDs is depicted in the top,  $q$  indicates the input qubit,  $S$  the two-qubit singlet state. Spin-dependent (red arrows) and energy-selective (teal arrows) tunneling are used for manipulating the register, lines 1-4 show the configuration after each step of the protocol. The two columns correspond to the classically distinguishable qubit states  $q = \uparrow$  (right) and  $q = \downarrow$  (left), in general, a superposition of the columns is obtained. A crossed-out arrow indicates suppressed tunneling. The final output qubit is found at the output site QD 2, highlighted in red. Step 4 is explained in more detail in Sec. III B 2 and Fig. 5.

the input qubit was in state  $|\uparrow_1\rangle$  and movement is suppressed if the input qubit was in state  $|\downarrow_1\rangle$ . In the second step, the energy-selective tunneling introduced above is performed for the transition from QD 2 to QD 1, then, in the third step, the energy-selective tunneling is repeated for the transition from QD 3 to QD 2.

QD 2 is declared the output site. If the input qubit was in state  $|\downarrow_1\rangle$ , all movements were suppressed and the original candidate qubit in state  $|\uparrow_2\rangle$  is still found in QD 2. However, if the input qubit was in state  $|\uparrow_1\rangle$ , both candidate qubits are shifted to the left by one site and QD 2 is populated by an electron in state  $|\downarrow_2\rangle$ . In general, the input qubit is in a superposition state, therefore a corresponding superposition of the final configurations is obtained. Finally, the population of QDs 0, 1, and 3 is discarded as described in Sec. III B 2 and the output qubit replaces the input qubit.

During every step of the operation, the basis states acquire a phase shift, the precise value depends on the microscopic parameters of the Hamiltonian and the protocol for each step. If uncompensated, the total operation has the effect of a gate sequence  $R_z(\phi)X$ , where  $R_z(\phi)$  is a rotation around the  $z$  axis of the Bloch sphere by an angle  $\phi$ , removing the phases with an  $R_z(-\phi)$  rotation

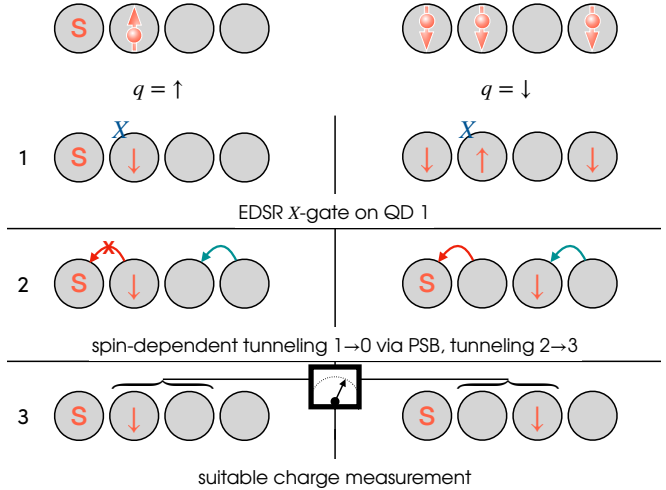


FIG. 5. Example of a disentangling operation for spin qubits following an  $X$  gate. The top row shows the final configuration of the QD array after the rearrangement from Fig. 4 for both input states, with the output qubit from QD 2 shuttled away. Steps 1 and 2 prepare a configuration where a single measurement is sufficient for the disentangling, the figure shows the configuration after each step. In step 3, the charge of QDs 1 and 2 is measured in the basis defined by  $(|1_1\rangle|x_2\rangle \pm |x_1\rangle|1_2\rangle)/\sqrt{2}$ , where  $1(x)$  indicates a QD occupied by one (zero) electrons. A measurement of the total charge occupation in QD 1 or 2 would be equivalent to measuring the output qubit.

results in an  $X$  gate. We note that only baseband controls are required for the implementation of rearrangement operation, which is beneficial to mitigate adverse heating effects [62, 63].

## 2. Disentangling Operation

As conclusion of the  $X$  gate presented in the previous section, the additional electrons need to be disentangled from the output qubit, otherwise enhanced dephasing is expected due to the vulnerability of the charge state against charge noise. One example of a disentangling operation is outlined in Fig. 5. The output qubit is not required for the disentangling operation, therefore we assume it is shuttled to a new destination while the disentangling commences, freeing up QD 2.

In the first step, the spin from QD 1 is flipped by an  $X$  gate performed with EDSR, which may be exploited to apply the phase compensation as virtual  $R_z(-\phi)$  rotation. Subsequently, another PSB operation in QDs 0 and 1 is executed, such that a singlet is formed in QD 0 also in the case of  $q = \downarrow$  as input state, while the energy offset of the three charges in the case  $q = \uparrow$  suppresses all movement. Simultaneously to the PSB, the population from QD 3 is shuttled to QD 2, both bucket brigade or conveyor mode shuttling are viable options. Now, the

two configurations differ only by the position of a single charge.

As discussed in Sec. II, a charge measurement in the basis  $\{\frac{1}{\sqrt{2}}(|1_1\rangle|x_2\rangle + |x_1\rangle|1_2\rangle), \frac{1}{\sqrt{2}}(|1_1\rangle|x_2\rangle - |x_1\rangle|1_2\rangle)\}$ , where  $1(x)$  indicates a QD occupied by one (zero) electron, is sufficient for disentangling the auxiliary qubits from the output qubit. This can be accomplished by adiabatically tuning the two QDs to resonance and measuring the population in one of the dots. The auxiliary qubits can then be discarded into a reservoir or reset. Due to the accumulation of phases during the first two steps and the non-deterministic outcome of the measurement, additional phases may be added to the output qubit, which can be removed with a physical  $R_z$  rotation.

We emphasize that this protocol is not unique. Other measurements may be favourable for the disentangling, depending on the chip layout, the measurement time compared to the duration of the charge and spin operations, and the measurement fidelity. In Sec. II it was shown that all errors on the discarded qubits translate into dephasing of the output qubit, thus operations which are not noise biased may be used, including the conventional quantum gates.

### 3. Two-Qubit CNOT Gate

A CNOT gate, up to phase corrections, can be designed following the same principles as the  $X$  gate. With two input qubits, candidate qubits to distinguish the four two-qubit basis vectors need to be prepared, doubling the required resources. One possible realization is shown in Fig. 6. The replacement-type CNOT gate uses the same techniques introduced in Sec. III A.

In the first quantum dot, QD 0, a reference spin for the control qubit in state  $|\downarrow_0\rangle$  is prepared, followed by the control qubit  $q_c$  in QD 1. Analogously, in QD 3 a reference spin  $|\downarrow_3\rangle$  for the target qubit is prepared, followed by the target qubit  $q_t$  in QD 4. The first step of the CNOT gate uses spin-selective tunneling from QD 1 to QD 0 and, in parallel, from QD 4 to QD 3. The PSB operations create a charge distribution conditional on  $(q_c, q_t)$ .

One candidate qubit is prepared in state  $|\uparrow_2\rangle$  in QD 2 and three further candidates are prepared in the state  $|\downarrow_5, \uparrow_6, \downarrow_7\rangle$  in QDs 5, 6 and 7. After the first step, all charges are moved up towards lower indexed QDs via energy-selective tunneling to close all gaps. Depending on  $(q_c, q_t)$ , the candidate qubits are moved up by two sites, one site, or all displacements are suppressed.

Finally, QD 1 is declared the output site for the control qubit, it thus is replaced by a superposition of the candidate qubit from QD 2 and the amplitude of  $q_c$  which was blockaded by the PSB. For the target qubit, QD 5 is chosen as output site. If the spin projections of  $q_c$  and  $q_t$  are anti-aligned, the charges are moved up by one site and  $|\uparrow_5\rangle$  is found, otherwise the spin state is  $|\downarrow_5\rangle$ . Therefore,

the replacement-type gate reproduces the truth table of a CNOT gate, although, as with the single-qubit gates, each basis state acquires a unique phase during the time evolution, which may need to be compensated. Again, the gate should be followed by a disentangling operation, entailing a measurement of the charge configuration in a suitable basis.

We note that closing the gaps requires the energy-selective displacement of a two-electron singlet in the case  $(q_c, q_t) = (\uparrow, \uparrow)$ . This may be experimentally challenging but can be circumvented by separating the double-occupied charge state before the tunneling into a laterally adjacent empty QD, if the array is not strictly linear. Alternatively, a sequence of three PSB events may be used, each immediately followed by a chain of energy-selective tunneling events: from QD 1 to QD 0, then from QD 3 to QD 2, then from QD 4 to QD 3. This way, the singlet state is created in its final position, however, the duration of the gate is increased, and the final PSB step needs to be energy-selective such that tunneling is suppressed if QD 2 is double-occupied, or another qubit  $|\downarrow_8\rangle$  needs to be appended.

Entangling a fresh auxiliary qubit with an existing qubit is possible with considerably less overhead than the CNOT gate between two qubits in arbitrary states. This is achieved with a modification of the  $X$  gate protocol from Fig. 5: The populations of both QDs 1 and 2 are chosen as output, only the population of QDs 0 and 3 are disentangled with a suitable measurement. If the population in QD 1 is kept instead of the original qubit  $q$  and the population of QD 2 is understood as a new qubit, the effect of the operation is equivalent to the gate  $\text{CNOT}_{1 \rightarrow 2}|q_1\rangle|0_2\rangle$ , up to phase corrections. The auxiliary qubit from QD 2 could then be used as reference or candidate in a replacement-type gate on another qubit in a form of entanglement swapping. This may facilitate a more efficient implementation of the syndrome-measurements in quantum error correction compared to the general replacement-type CNOT gate.

### C. Discussion of Error Mechanisms

The replacement-type gates for spin qubits primarily rely on two physical mechanisms, Pauli spin blockade and energy-selective tunneling. A number of errors can lead to a candidate qubit with the incorrect spin state (bit error), or even no qubit at all in the output site (charge error).

A major source of bit errors is the lifting of the spin blockade, allowing other two-particle states than the intended one to be merged into a single quantum dot. This can be caused by spin-flip processes,  $t_{i,j,\uparrow,\downarrow}$ ,  $t_{i,j,\downarrow,\uparrow}$  in Eq. (11), which may emerge due to synthetic or intrinsic SOI [64, 65]. Furthermore, a low-lying orbital state, the excited valley state for electrons in silicon or bilayer graphene, in particular, can lead to an available triplet state in the double-occupied dot [66–68]. Relaxation of

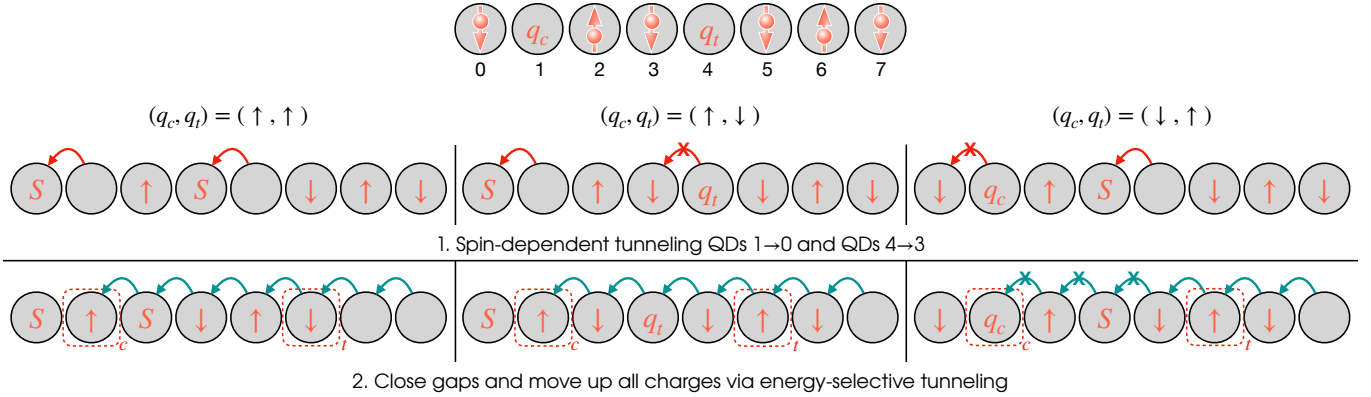


FIG. 6. Protocol for a replacement-type CNOT gate for spin qubits. The top row shows the initial configuration of the input, candidate, and reference qubits, the following rows show the possible configurations after the described operation. The label  $q_{c(t)}$  indicates the control (target) qubit. The columns correspond to different two-qubit basis states  $(q_c, q_t)$ . Output sites for the new control ( $c$ ) and target ( $t$ ) qubit are highlighted in the bottom row. The desired final state is prepared by two parallel spin-dependent tunneling events, followed by moving up all qubits from left to right. In the case  $(\downarrow, \downarrow)$ , which is not shown, all movement is suppressed.

the excited spin state before or during the tunneling process will also result in an error, but is highly unlikely due to the long spin lifetime. Finally, a non-adiabatic sweep of the detuning leads to Landau-Zener (LZ) transitions between the instantaneous eigenstates, resulting in the undesired outcome where the population of an unblockaded state remains in its charge configuration [69, 70].

LZ transitions are a leading error mechanism of the energy-selective tunneling with a single electron as well. A non-adiabatic sweep with respect to the spin-conserving tunneling can result in cases where the electron is left behind, potentially in combination with a spin flip or valley excitation [54]. Of particular relevance is the regime  $(B_i + B_j)/2 > 2|t_{i,j,\sigma,\sigma}|$  with a non-zero spin-flip tunneling, where different paths of adiabatic and non-adiabatic transitions through the sequence of ALCs lead to the same outcome. Depending on the relative phase accumulated between the ALCs constructive or destructive interference between these paths may emerge [54, 71].

The energy selective tunneling may suffer from leakage, allowing tunneling also for the states with two electrons in the two QDs if the charging energy  $U_2 - U_1 \gg |t_{i,j,\sigma,\sigma}|$ . This can be understood from Fig. 3: Traversing the single-electron ALCs may bring the system in the vicinity of the two-electron ALCs, where the single- and double-occupied states hybridize.

Further imperfections which are reflected as bit errors arise from the erroneous preparation of the reference and candidate qubits. As discussed in Sec. II, errors during the disentangling operation, including measurement errors, result in phase errors.

Throughout all operations, the qubits experience dephasing (phase errors) due to low-frequency fluctuations of the energy levels caused by electric charge noise, the coherences of the charge state are particularly vulnerable [20, 21]. The rapid dephasing due to charge noise

favors fast detuning sweeps during the gate, therefore, a trade-off between adiabaticity and dephasing is anticipated [55]. Furthermore, even in the regime of an adiabatic detuning sweep for the energy-selective tunneling, LZ transitions induced by charge noise can cause the electron to be left behind, fundamentally limiting the noise bias of the gate [71, 72].

We note that at no point the qubit state is manipulated by a spin rotation, neither are the basis vectors temporarily relabelled. This eliminates the direct translation of the dominant phase errors stemming from charge noise into bit errors. We further note that the mechanisms for bit and charge errors are largely insensitive to the phase of the spins. It is possible for phase errors to impact the spin projection and charge distribution if the energy-selective tunneling is performed in a non-adiabatic regime where the probability amplitudes for different paths in the level diagram can interfere due to LZ transitions. However, this interference can be strongly suppressed by choosing  $2|t_{i,j,\sigma,\sigma}| > (B_i + B_j)/2$  and a sufficiently adiabatic level velocity of the detuning sweep [54, 71].

The phase of the spin state can in general impact the PSB: The singlet state  $|S_{(1,1)}\rangle$  is mapped to the triplet state  $|T_0\rangle$  and vice versa by a phase flip on one of the spins. In our proposed protocol, however, a longitudinal magnetic gradient is used, in the presence of which the singlet and triplet states are no eigenstates anymore. Instead, the relevant two-spin states are  $(|S_{(1,1)}\rangle \pm |T_0\rangle)/\sqrt{2}$ , for which a phase flip results in a global phase. Therefore, the translation of phase to bit errors in the PSB can be suppressed by choosing a sufficiently strong magnetic field gradient.

#### D. Quantum Process Tomography

From the discussion of the error mechanisms and the translation of errors, we expect that bit errors of the replacement-type gate are strongly suppressed if the detuning sweeps are sufficiently adiabatic and if the singlet-triplet splitting and on-site charging energy are sufficiently large. Therefore, we expect the replacement-type gate to be strongly noise-biased, dominated by phase errors. We confirm the noise bias by simulating quantum process tomography [73–75] for both the replacement-type  $X$  and CNOT gates. The disentangling operation, which contributes only phase errors, is not included in the simulation in order to study the error of the rearrangement operation alone.

The simulation is based on the Hamiltonian from Eq. (11), including the single-occupied states with both spin projections for all QDs, the empty state for all QDs except the leftmost one and the double-occupied singlet state and the lowest triplet state for all QDs except the rightmost one. We assume that the triplet state lies  $E_{\text{ST}} = 200 \mu\text{eV}$  above the singlet.

We extract the parameters of electron spin qubits in Si/SiGe from recent literature [56, 76–79]. For the PSB, we follow the procedure of Ref. [79], slowing down the detuning sweep to a level velocity of  $100 \mu\text{eV ns}^{-1}$  near the ALC and using a fast ramp with a level velocity of  $20 \text{meV ns}^{-1}$  away from the sensitive spots, in order to shorten the duration. With a spin-conserving tunnel coupling  $t_{i,j,\sigma,\sigma} = 25 \mu\text{eV}$  and a spin-flip tunneling  $t_{i,j,\sigma,\sigma'} = 0.25 \mu\text{eV}$ ,  $\sigma \neq \sigma'$ , this allows for a highly adiabatic and rapid PSB. We further assume a charging energy  $U_2 - U_1 = 5 \text{meV}$  and a longitudinal magnetic field gradient  $B_j - B_{j+1} = 10 \mu\text{eV}$ . As non-unitary sources of error we assume imperfect initialization with success probability  $p_i = 1 - 10^{-3}$ , dephasing of the spin state with  $T_2 = 20 \mu\text{s}$  and the charge state with  $T_{2,c} = 25 \text{ns}$ , and a spin relaxation time  $T_1 = 1 \text{s}$ .

In Fig. 7(a) we show simulated quantum process tomography for the replacement-type  $X$  gate. With the realistic parameters, bit errors occur with a probability one order of magnitude lower than phase errors, and are mostly caused by erroneous initialization of the reference and candidate qubits. Assuming a perfect initialization of all qubits,  $p_i = 1$ , the probability of bit errors is further suppressed by one order of magnitude. Further assuming a perfect PSB, slightly reduces  $x$ -errors and suppresses charge errors, which are generally on a very low level. The remaining errors are due to dephasing and imperfections in the energy-selective tunneling. The effect of spin relaxation is negligible.

In Fig. 7(b), the same is shown for the replacement-type CNOT, where a similar behavior is observed. Here, the effect of the bit errors related to PSB is stronger compared to the  $X$  gate, which is explained by the use of multiple PSB operations in the gate. Again, charge errors occur with a very low probability, slightly more likely on the target ( $c_t$ ), which is moved considerably more than

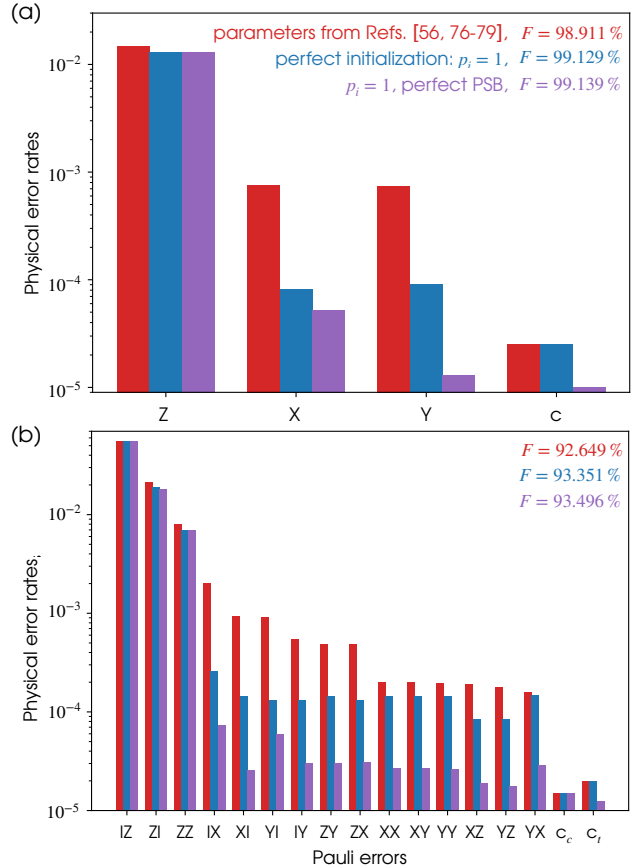


FIG. 7. Quantum process tomography of a simulated replacement-type  $X$  (a) and CNOT gate (b) with spin qubits, not including the disentangling operation. The bar diagram illustrates the probability of the Pauli and charge ( $c$ ) errors on the involved qubits, the fidelity  $F$  for each case is shown in the top right corner. In red the parameters discussed in the main text are used, in blue a perfect initialization is assumed,  $p_i = 1$ , and in purple the PSB is assumed to be error-free in addition to  $p_i = 1$ . Phase errors dominate throughout, initialization and PSB imperfections are a major source of bit errors but contribute hardly to phase errors. Charge errors occur with a very low probability.

the control ( $c_c$ ) qubit. Note that for the CNOT gate we assumed a larger tunneling in order to accommodate for  $2|t_{i,j,\sigma,\sigma}| > (B_i + B_j)/2$  throughout the longer QD array.

The results from quantum process tomography illustrate that the noise bias of the rearrangement operation can approach the ratio known for idling spin qubits, although a reduction of the errors of the spin initialization and spin-selective tunneling is required. We note that both techniques are based on PSB, where the fidelity can be enhanced by optimal control techniques [80, 81], by optimizing the confinement potential, and by engineering the valley splitting. The latter can be achieved by optimizing the width of the quantum well and the interfaces [82, 83] or by introducing germanium into the silicon quantum well [84–87].

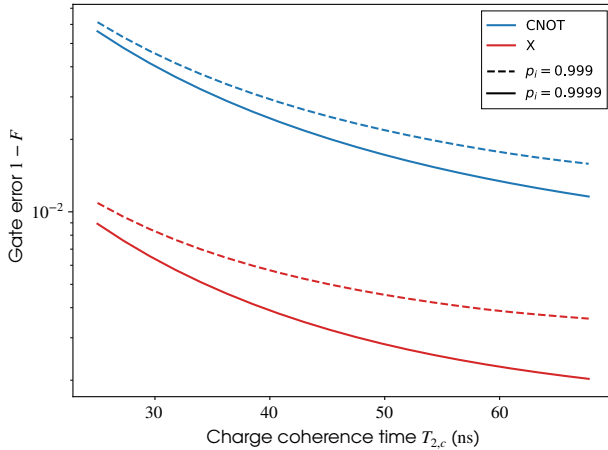


FIG. 8. Infidelity  $1 - F$  of replacement-type  $X$  (red) and CNOT (blue) gates with spin qubits as a function of the decoherence time  $T_{2,c}$  of the charge state. Solid lines correspond to a probability for correct initialization of  $p_i = 0.9999$  and dashed lines to  $p_i = 0.999$ , the other parameters are identical to Fig. 7, where  $T_{2,c} = 25$  ns was used. Extending the coherence to  $T_{2,c} = 70$  ns allows a CNOT fidelity as high as  $\approx 0.989$  and an  $X$  gate fidelity of  $\approx 0.998$ .

In our model, the fidelity of the replacement-type gate is limited by dephasing, in particular of the hybrid spin-charge state. In Fig. 8 we investigate the dependence of the infidelity on the charge coherence time  $T_{2,c}$  of the charge state. We find that with a sufficiently high initialization fidelity and with an extended  $T_{2,c}$ , a CNOT gate infidelity  $\lesssim 10^{-2}$  is possible. Extending  $T_{2,c}$  requires suppression of the environmental charge noise, which is challenging in practice. However, recent research is advancing the understanding of the microscopic origin of charge noise such that a noise reduction through adaptations of the device design is conceivable [22–25] and reduction strategies can be developed [63, 88, 89].

We emphasize that the parameters of the Hamiltonian here are not specifically optimized for the performance of the replacement-type gate. We expect that significant improvements can be achieved by finding an optimal regime for the magnetic field gradient which impacts PSB, the energy-selective tunneling, and the susceptibility of the spin state to charge noise. Uniformly displacing the entire register between regions of different gradients with conveyor mode shuttling may even allow tailoring its value to each operation. Optimizing the shape of the detuning ramps with optimal control theory is expected to bring further enhancement.

#### IV. REALIZATION WITH NEUTRAL ATOM QUBITS

The idea of the replacement-type gates can be extended to other qubit platforms, such as atoms or molecules. For concreteness, we here focus on neutral

atom qubits in optical tweezers that have shown significant progress for quantum computational tasks due to their versatile properties, including scalability in qubit count, and long-range interactions mediated by mid-circuit shuttling. In our proposed setup, the atoms are trapped using optical tweezers created by focused laser beams, and their internal states are manipulated through additional laser-driven transitions. Exciting these atoms to Rydberg states, highly excited electronic states with large principal quantum numbers, not only enables strong, tunable interactions for implementing entangling gates, but also facilitates controlled tunneling. This controlled tunneling plays a key role in realizing replacement-type gates via occupation-dependent tunneling and state-dependent tunneling.

For concreteness, we focus on the fermionic isotope of Alkaline-earth(-like) atoms possessing large nuclear spin  $I$  (such as  $^{87}\text{Sr}$  with  $I = 9/2$  and  $^{173}\text{Yb}$  with  $I = 5/2$ ) where quantum information is encoded in the nuclear spin of the low-lying electronic states [90, 91]. The electronic ground state  $^1\text{S}_0$  and the metastable clock state  $^3\text{P}_0$  are of particular interest as they feature a rich subspace due to Zeeman splitting. These hyperfine sublevels  $|m_F\rangle$  are dominantly characterized by the nuclear spin  $F = I$  as the total electronic angular momentum  $J$  is zero. As a result, the nuclear spin demonstrates very long coherence times up to the order of seconds [92, 93]. The rich internal structure allows for various qubit modalities [94] and enables versatile qudit-based simulations of complex Hamiltonians such as lattice gauge theories [95, 96].

We utilize the Rydberg manifold  $^3\text{S}_1$  passing through the metastable excited manifold  $^3\text{P}_0$  to activate interactions between atoms. The strong Van der Waals (VdW) interaction between nearby atoms is the main resource to implement entangling gates, such as controlled- $Z$  gates, via the so-called Rydberg Blockade mechanism. Moreover, the Rydberg manifold  $^3\text{S}_1$ , in contrast to the ground and metastable manifold, possesses non-zero  $J = 1$  and therefore strong hyperfine coupling. Consequently, a magnetic field strongly splits the Zeeman sublevels of the Rydberg manifold. This allows selective addressing of the sublevels, which is crucial for our Rydberg-based gate operations. The following will explain how this level structure enables the conditional operations required for the replacement-type gates.

The details of our scheme are illustrated in Fig. 9. The atomic level structure comprises a ground manifold in which the qubit is encoded in the stretched nuclear spin states with  $|0\rangle$  and  $|1\rangle$ , corresponding to  $|^1\text{S}_0, F = \mp m_F = \mp I\rangle$ , respectively. Coherent population transfer to the metastable clock state  $^3\text{P}_0$  is achieved using a two-tone  $\pi$ -pulse that simultaneously drives the clock transitions  $|0\rangle \rightarrow |e_+\rangle$  and  $|1\rangle \rightarrow |e_-\rangle$ , where  $|e_{\mp}\rangle \equiv |^3\text{P}_0, F = \mp m_F = \mp I\rangle$ . Each frequency component of the pulse is tuned to be resonant with its respective  $m_F \rightarrow m'_F$  transition, ensuring state-selective excitation without cross-talk.

Excitation from the metastable to the Rydberg man-

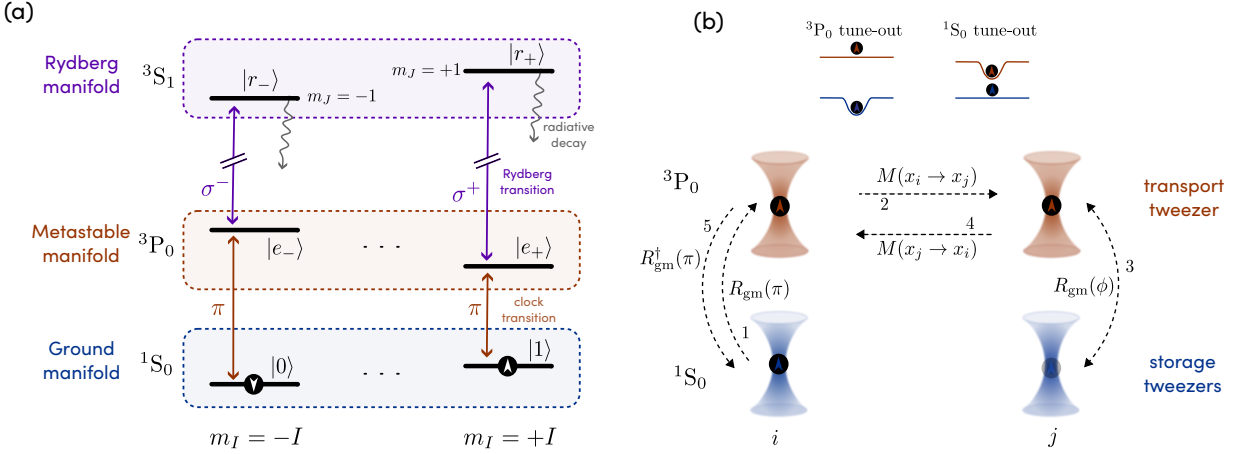


FIG. 9. (a) Qubit states are encoded in the stretched nuclear spin states located at the edges of the total magnetic quantum number within the ground manifold, specifically  $|0\rangle \equiv |^1S_0, F = -m_F = I\rangle$  and  $|1\rangle \equiv |^1S_0, F = m_F = I\rangle$ , which are interchangeably referred to as  $|\downarrow\rangle$  and  $|\uparrow\rangle$ , respectively. A dual-tone optical  $\pi$ -pulse addresses the clock transition to the metastable manifold  $^3P_0$  for both qubit levels, namely  $|0\rangle \leftrightarrow |e_-\rangle$  and  $|1\rangle \leftrightarrow |e_+\rangle$ . The metastable state serves two purposes: It enables transport of the atom via tweezers that selectively trap  $^3P_0$  while being tuned out for  $^1S_0$ , and it acts as an intermediate state to Rydberg excitation for entangling gates. With stretched Rydberg states defined as  $|r_\mp\rangle \equiv |^3S_1, F = \mp m_F = I + 1\rangle$ , the required Rydberg coupling is achievable via  $\sigma^\mp$ -polarized UV light. (b) Shuttling protocol utilizing state-selective trapping: Two static storage tweezers positioned at sites  $i$  and  $j$  (blue) confine atoms in the ground state while being tuned out for  $^3P_0$ , and a mobile transport tweezer (orange) shuttles atoms in  $^3P_0$  between the two. As an example, suppose the tweezer at site  $i$  holds an atom in  $|0\rangle$ , and site  $j$  is initially unoccupied. The transport tweezer is then turned on at site  $i$ , followed by a  $\pi$  pulse  $R_{gm}(\pi)$  that maps  $|0\rangle \rightarrow |e_-\rangle$ , loading the atom into the mobile tweezer. After moving to site  $j$ , a  $R_{gm}(\phi)$  operation redistributes population into the storage tweezer at site  $j$ , depending on the angle  $\phi$ . The transport tweezer returns to site  $i$ , and a final  $R_{gm}^\dagger(\pi)$  operation transfers the remaining population back to the ground state, creating a spatial superposition of  $|0\rangle$  or vacuum. This sequence effectively realizes a hopping of a particular qubit state between sites  $i$  and  $j$ .

ifold is performed via another dual-tone laser field that couples the states  $|e_\mp\rangle$  to the stretched Rydberg states  $|r_\mp\rangle \equiv |^3S_1, F = \mp m_F = I + 1\rangle$ . These transitions are selected to obey electric dipole selection rules and are driven with matched Rabi frequencies, maintaining symmetry between the two qubit excitation pathways. This configuration enables coherent and independent manipulation of the two qubit states while significantly suppressing undesired coupling between the subspaces  $\{0, e_-, r_-\}$  and  $\{1, e_+, r_+\}$ , which lie at the extremal values of the  $m_F$  manifold. The isolation of these stretched states minimizes bit-flip errors and is a key design feature that supports the implementation of noise-bias-preserving replacement-type gates.

### A. Required Operations

The gate protocols rely on two key primitives: state-dependent tunneling and state-dependent Rydberg interactions. Tunneling is implemented using two types of optical tweezers: (i) deep storage tweezers, which localize atoms in the ground state at fixed lattice sites, and (ii) transport tweezers, which enable controlled shuttling of atoms between sites. For Rydberg-mediated interactions, site-resolved, multi-tone laser fields are used to selectively excite atoms depending on their internal state, facilitating controlled, state-dependent coupling between

atoms.

#### 1. State-dependent trapping

Optical tweezers confine atoms through the AC Stark effect, where a red-detuned laser induces a potential well that draws atoms toward regions of maximum intensity [97]. Since the AC Stark shift depends on the atomic polarizability, internal states with differing polarizabilities experience distinct trapping potentials, a phenomenon known as state-dependent trapping. This effect is particularly pronounced in alkaline-earth-like atoms, where the polarizabilities of the  $^1S_0$  ground state and the metastable  $^3P_0$  state differ significantly across the optical spectrum, owing to their distinct electronic structures and resonance features [98, 99]. Consequently, specific laser wavelengths can be selected such that one state is strongly trapped while the other remains only weakly confined or untrapped. Detailed analyses of suitable wavelengths for  $^{87}\text{Sr}$  and  $^{173}\text{Yb}$  are available in Ref. [100]. Unlike alkali atoms, the narrow linewidth of the clock transition  $^1S_0 \rightarrow ^3P_0$  in these species significantly suppresses spontaneous emission to the ground state manifold.

In what follows, we describe a shuttle gate mechanism based on state-dependent trapping, originally proposed in Refs. [96, 101]. In this scheme, a transport tweezer,

resonant with the metastable  ${}^3P_0$  manifold, is dynamically moved between two sites defined by storage tweezers, which are tuned to trap atoms in the  ${}^1S_0$  ground manifold. This allows for coherent spatial transport of atoms conditional on their internal quantum state. It is important to point out that despite the high accuracy achievable with these shuttling operations, they are considerably time-consuming relative to other coherent processes. However, advancements in technique offer potential for accelerating atom transport [102, 103].

The qubit is initially prepared in an arbitrary superposition of the ground manifold states  $|0\rangle$  and  $|1\rangle$ , confined by a static optical tweezer at position  $x_i$ . To enable state-dependent transport, a second (transport) tweezer is introduced and aligned with the storage tweezer at  $x_i$ . A resonant  $\pi$ -pulse drives the population in  $|1\rangle$  to the excited state  $|e_+\rangle$ , leaving  $|0\rangle$  unchanged. At this point, the atom experiences a combined potential from both tweezers. The transport tweezer is then spatially displaced, separating the trapping potentials and mapping the internal superposition onto a spatial superposition. The component in  $|e_+\rangle$  is transported to a new location  $x_j$ , denoted by the operation  $M_{x_i \rightarrow x_j}$ . At this position, an X-rotation  $R_{\text{gm}}^{\uparrow}(\phi)$  is applied between  $|1\rangle$  and  $|e_+\rangle$ , followed by returning the transport tweezer to its original location  $x_i$  ( $M_{x_j \rightarrow x_i}$ ). Finally, a de-excitation  $\pi$ -pulse  $(R_{\text{gm}}^{\uparrow})^{\dagger}(\pi)$  maps  $|e_+\rangle$  back to  $|1\rangle$ , completing the sequence.

In summary, the shuttle gate sequence described above implements the following unitary operation:

$$T_{i,j}^{\alpha}(\phi) = (R_{\text{gm}}^{\alpha})^{\dagger}(\pi) M_{x_i \rightarrow x_j} R_{\text{gm}}^{\alpha}(\phi) M_{x_j \rightarrow x_i} R_{\text{gm}}^{\alpha}(\pi), \quad (12)$$

where  $\alpha = \uparrow$  corresponds to the case where the population in  $|1\rangle$  is excited to the metastable state  $|e_+\rangle$ , as in the example provided. More generally,  $\alpha$  can take the value  $\uparrow$  or  $\downarrow$ , depending on whether the metastable state  $|e_+\rangle$  or  $|e_-\rangle$  is used to shuttle the population from  $|1\rangle$  or  $|0\rangle$ , respectively. This sequence realizes a tunneling unitary of the form:

$$T_{i,j}^{\alpha}(\phi) = e^{-i\frac{\phi}{2}((c_i^{\alpha})^{\dagger}c_j^{\alpha} + \text{H.c.})}, \quad (13)$$

where  $c_i^{\alpha}$  is the fermionic annihilation operator associated with internal state  $\alpha$  at site  $i$ . The parameter  $\phi$ , set by the rotation angle in the third step of the sequence, determines the strength of the coherent tunneling between sites  $i$  and  $j$ .

## 2. State-Dependent Interactions

An essential building block for entangling operations is the use of VdW interactions. These interactions arise when atoms are excited to high-lying Rydberg states of identical parity, enabling strong VdW coupling. When two atoms are positioned within the so-called Rydberg blockade radius, simultaneous excitation to the Rydberg state becomes energetically forbidden. This Rydberg

blockade mechanism is widely used to implement entangling gates in neutral atom platforms.

In alkaline-earth-like atoms, direct one-photon excitation to the Rydberg manifold is feasible using UV laser light. The excitation can be shaped via phase modulation to implement a two-body interaction of the form  $e^{-i\theta n_i n_j}$ , where  $n_i$  and  $n_j$  represent the occupation number operators of the Rydberg states on atoms  $i$  and  $j$ , respectively [31]. In this work, we set  $\theta = \pi$  to realize a maximally entangling phase gate.

We further assume that Rydberg excitation is state-selective: Depending on the internal states  $\alpha$  and  $\beta$  of atoms  $i$  and  $j$ , respectively, the entangling gate is described by

$$E_{i,j}^{\alpha,\beta} = e^{-i\pi n_i^{\alpha} n_j^{\beta}}, \quad (14)$$

where  $n_i^{\alpha}$  and  $n_j^{\beta}$  denote the occupation numbers of states  $\alpha$  and  $\beta$ , with  $\alpha, \beta \in \{\uparrow, \downarrow\}$ , corresponding to Rydberg states  $|r_+\rangle$  and  $|r_-\rangle$ , respectively. For example, when both atoms are excited to the  $|r_+\rangle$  state, the interaction becomes:  $E_{i,j}^{\uparrow,\uparrow} = e^{-i\pi n_i^{\uparrow} n_j^{\uparrow}}$ . Alternatively, if atom  $i$  is driven to  $|r_+\rangle$  and atom  $j$  to  $|r_-\rangle$  via independently addressable lasers, the resulting interaction is:  $E_{i,j}^{\uparrow,\downarrow} = e^{-i\pi n_i^{\uparrow} n_j^{\downarrow}}$ .

Moreover, VdW interactions can be harnessed to realize multi-qubit entangling gates. This can be achieved by positioning atoms within the blockade radius and employing optimal control techniques to shape the driving fields for implementing a desired unitary operation (see, for example, [104–106]). Extending the procedure for the two-qubit entangling gate in Eq. (14), state-selective excitation to the Rydberg manifold also enables the implementation of an internal-state-dependent three-qubit entangling gate, which takes the form

$$E_{i,j,k}^{\alpha,\beta,\gamma} = e^{-i\pi n_i^{\alpha} n_j^{\beta} n_k^{\gamma}}. \quad (15)$$

In the following section, we will utilize these primitive operations to construct replacement-type gate structures.

A practical challenge in Rydberg-based gates is spontaneous decay from the Rydberg manifold, as the Rydberg lifetimes are comparable to typical gate durations. This decay constitutes a major source of noise [32]. To mitigate its effect and preserve the noise bias in our gate design, we utilize stretched Rydberg states. Due to selection rules, transitions from  $|r_+\rangle$  to states with negative magnetic quantum number  $m_I$  are strongly suppressed, and similarly for  $|r_-\rangle$  with positive  $m_I$ , thereby reducing undesired decay channels. A similar approach for alkali atoms is introduced in Ref. [18].

## 3. Occupation-Controlled Tunneling Gates

Occupation-controlled tunneling gates can be engineered by combining state-dependent tunneling with state-dependent entangling operations. These composite

gates enable conditional tunneling based on the occupation of one or more control sites. The gate constructions are adapted from Ref. [101]. Note that in this work, we focus only on atom trapping using optical tweezers for brevity. However, similar gate operations can also be realized in optical lattice platforms for example, by tilting the lattice and leveraging collisional interactions, as demonstrated in [107].

*a. Single-Site Control* The gate  $C_i^\alpha T_{j,k}^\beta$  implements a tunneling operation for an atom in internal state  $\beta$ , interpreted as  $|0\rangle$  for  $\beta = \downarrow$  and  $|1\rangle$  for  $\beta = \uparrow$ , from site  $j$  to site  $k$ , conditioned on the atom at site  $i$  being in internal state  $\alpha$ . This gate can be realized by the following sequence:

$$C_i^\alpha T_{j,k}^\beta = T_{j,k}^\beta(\pi/2) E_{i,j}^{\alpha,\beta} T_{j,k}^\beta(-\pi/2) E_{i,j}^{\alpha,\beta}. \quad (16)$$

In this sequence, the entangling gates act to modify the effective sign of the intermediate tunneling operation when the control condition is satisfied. The overall effect of the sequence is to apply a tunneling operator conditioned on the occupation of site  $i$ , which can be expressed more compactly as:

$$C_i^\alpha T_{j,k}^\beta = e^{-i\frac{\pi}{2}((c_j^\beta)^\dagger n_i^\alpha c_k^\beta + \text{H.c.})}. \quad (17)$$

*b. Two-Site Control* The conditional logic can be extended to cases involving two control sites. The gate  $C_{i,j}^{\alpha,\beta} T_{i,j}^\gamma$  enables tunneling of a particle in internal state  $\gamma$  between sites  $i$  and  $j$ , but only if site  $i$  is occupied by an atom in state  $\alpha$  and site  $j$  by an atom in state  $\beta$ . The gate is constructed via the sequence:

$$C_{i,j}^{\alpha,\beta} T_{i,j}^\gamma = T_{i,j}^\gamma(\pi/2) E_{i,j}^{\alpha,\beta} T_{i,j}^\gamma(-\pi/2) E_{i,j}^{\alpha,\beta}. \quad (18)$$

This structure allows the tunneling to occur only if both control site conditions are satisfied. In contrast, one may also construct a gate that triggers tunneling in the absence of a specific two-site configuration. The gate  $C_{i,j}^{\neg(\alpha,\beta)} T_{i,j}^\gamma$  permits tunneling only if site  $i$  is not in state  $\alpha$  or site  $j$  is not in state  $\beta$ . This is implemented by:

$$C_{i,j}^{\neg(\alpha,\beta)} T_{i,j}^\gamma = T_{i,j}^\gamma(\pi/2) E_{i,j}^{\alpha,\beta} T_{i,j}^\gamma(\pi/2) E_{i,j}^{\alpha,\beta}. \quad (19)$$

Here, unlike in Eq. (18), both tunneling gates carry the same phase, thereby altering the constructive interference condition based on the control occupation.

*c. Generalization to Non-Local Control* This conditional tunneling framework can be generalized further to allow for spatial separation between the control and tunneling regions. Specifically, the tunneling of an atom between two arbitrary sites  $k$  and  $l$  can be conditioned on the internal states of two different control sites  $i$  and  $j$ . This is made possible using the three-body, internal-state-dependent entangling gate introduced earlier. The corresponding gate construction is:

$$C_{i,j}^{\alpha,\beta} T_{k,l}^\gamma = T_{k,l}^\gamma(\pi/2) E_{i,j,k}^{\alpha,\beta,\gamma} T_{k,l}^\gamma(-\pi/2) E_{i,j,k}^{\alpha,\beta,\gamma}. \quad (20)$$

This generalization greatly enhances the flexibility of occupation-controlled dynamics and enables the design of more complex gate architectures in neutral atom platforms [95, 108].

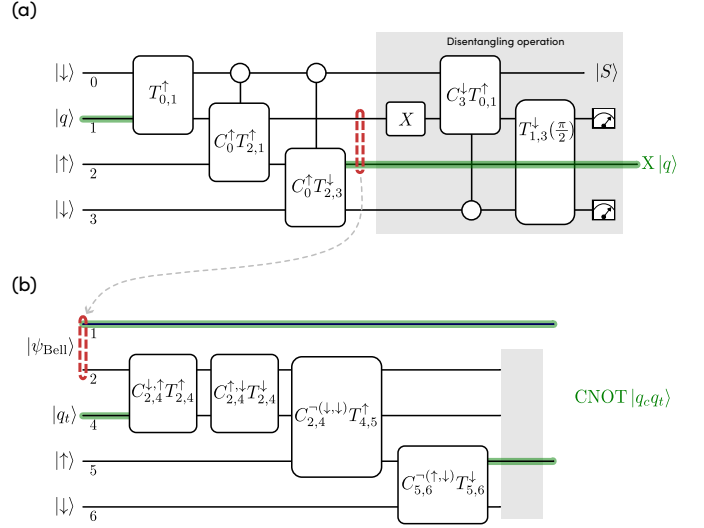


FIG. 10. (a) A tunneling-assisted protocol for the implementation of the noise-biased  $X$  gate on a neutral atom platform. Here, the occupation-controlled tunneling is performed via state-dependent tunneling and Rydberg entangling gates. The first three gates convert an input qubit at site 1 into the desired state  $X|q\rangle$  at site 2, and the remaining gates (gray box) disentangle the auxiliary qubits 0, 1, and 3 from the output qubit. (b) The protocol for the CNOT gate based on the Bell state from the previous circuit at sites 1 and 2 (red dashed line). Here, sites 1 and 4 represent the control and the target qubits respectively, and sites 5 and 6 represent additional candidate qubits. The depicted four conditional tunneling gates generate the desired state  $\text{CNOT}|q_c q_t\rangle$  at sites 1 and 5, and the remaining qubits can then be discarded after a subsequent disentangling operation.

## B. Implementations of Replacement-Type Gates

With the set of primitive operations introduced in the previous section, we are now equipped to provide concrete protocols for realizing replacement-type gates with neutral-atom qubits. These protocols demonstrate how approximately noise bias-preserving single- and two-qubit gates can be constructed using the available gate primitives. In the following, we outline explicit sequences for the implementation of an  $X$  gate and a CNOT gate, focusing on their realization via spatially-resolved atomic manipulation in optical tweezers.

### 1. Single-Qubit $X$ Gate

A protocol for realizing the  $X$  gate is shown in Fig. 10(a). In analogy to the protocol used for spin-based qubit platforms in Secs. III B 1, III B 2 we employ four storage tweezers loaded as  $|\Psi_{\text{in}}\rangle = |\downarrow_0, q_1, \uparrow_2, \downarrow_3\rangle$  representing the reference, input, and two candidate qubits, respectively. Here,  $|q\rangle = \alpha_\downarrow |\downarrow\rangle + \alpha_\uparrow |\uparrow\rangle$  is an arbitrary state of the input qubit. The bias-preserving  $X$  gate is implemented through a sequence of conditional tunneling

steps that selectively merge the spatially separated candidate states into an output qubit, generating the desired output qubit  $X|q\rangle$ .

The procedure relies on occupation-controlled tunneling of internal states, and proceeds as follows: First, a state-dependent tunneling operation  $T_{0,1}^\uparrow$  is applied, enabling coherent transfer of the  $|\uparrow\rangle$  state between sites 0 and 1 via a transport tweezer. This step selectively transfers the  $\uparrow$  component of the input qubit to site 0. This prepares the system for controlled routing based on the initial qubit state. Next, a controlled tunneling gate  $C_0^\uparrow T_{2,1}^\uparrow$  is applied, enabling the  $|\uparrow\rangle$  state to tunnel from site 2 to site 1 if and only if site 0 contains an atom in the  $|\uparrow\rangle$  state. Otherwise, the candidate qubit at site 2 remains unaffected, effectively encoding a bit-flipped version of the  $\downarrow$  component of the input qubit. A similar conditional operation  $C_0^\uparrow T_{2,3}^\downarrow$  is applied to transfer the  $|\downarrow\rangle$  state from site 3 to site 2, again conditioned on the presence of a  $|\uparrow\rangle$  atom at site 0. This step completes the state transformation necessary to enact the  $X$  gate behavior at site 2.

At this stage, auxiliary atoms located at sites 0, 1, and 3 are no longer needed and are discarded. Only the output atom, located at site 2, carries the desired state. Disentangling the output qubit from the rest requires extra gates, while keeping the output qubit intact. One possible disentangling operation contains a sequence of three primitive gates. First, an  $X$  gate is applied on qubit 1, which is then followed by a controlled tunneling gate  $C_3^\downarrow T_{0,1}^\uparrow$  resulting in the formation of a singlet state in site 0, i.e.  $|S_0\rangle = (c_0^\uparrow)^\dagger (c_0^\downarrow)^\dagger |x\rangle$ , and  $|\downarrow\rangle$  state in site 2 or 3. Note that the  $X$  gate here does not need to preserve the noise bias, as discussed in Sec. II. Now, applying  $T_{1,3}^\downarrow(\frac{\pi}{2})$  makes an equally weighted superposition of a single spin-down atom shared between sites 1 and 3. Finally, by performing only a single spin-down measurement in sites 1 or 3, the auxiliary qubits are completely disentangled from the output qubit and can be safely discarded or reused for other computational tasks.

This protocol leverages spatial degrees of freedom in addition to internal states to encode and manipulate quantum states, offering an alternative route toward bias-preserving gate implementation using neutral-atom platforms. Incorporating other degrees of freedom, such as the motional states, can also be used as a resource to implement or enhance the replacement-type gates by coherent conversion between electronic and motional states, see for example Ref. [109].

## 2. Two-Qubit CNOT Gate

The CNOT gate, a key two-qubit entangling operation, requires a more complex implementation compared to the single-qubit  $X$  gate. Beyond the basic  $X$  gate sequence described earlier, an additional entangling step is needed to ensure that the quantum state of a target qubit is

flipped conditionally, based on the state of the control qubit. To achieve this, we leverage the entangled state already present in the  $X$  gate sequence, namely  $|\psi_{\text{Bell}}\rangle = \frac{1}{\sqrt{2}}(\alpha_\downarrow |\downarrow_1\uparrow_2\rangle + \alpha_\uparrow |\uparrow_1\downarrow_2\rangle)$  as shown in Figure 10. We then incorporate conditional tunneling that depends on the state of the target qubit at site 4 and the bit-flipped version of the control qubit at site 2, along with two additional candidate qubits at sites 5 and 6 initialized in the state  $|\uparrow_5\downarrow_6\rangle$ . This functionality is enabled using the two- and three-site occupation-controlled tunneling gates introduced in Sec. IV A 3.

Figure 10(b) illustrates the key steps of the entangling protocol used to implement a bias-preserving CNOT gate. The sequence proceeds as follows: The first step involves state-dependent tunneling such that an atom in state  $|\uparrow\rangle$  tunnels between sites 2 and 4 only if the spins on those two sites are anti-aligned, i.e., in configurations  $|\downarrow_2\uparrow_4\rangle$  or  $|\uparrow_2\downarrow_4\rangle$ . This is achieved by sequentially applying the two-site controlled tunneling gates  $C_{2,4}^{\downarrow,\uparrow} T_{2,4}^\uparrow$  and  $C_{2,4}^{\uparrow,\downarrow} T_{2,4}^\downarrow$ , which respectively enable tunneling of the  $|\uparrow\rangle$  and  $|\downarrow\rangle$  states from site 4 to site 2 under the corresponding anti-aligned spin conditions.

Now, the three-site gate  $C_{2,4}^{-(\downarrow,\uparrow)} T_{4,5}^\uparrow$  is applied to move the  $|\uparrow\rangle$  state from site 5 to site 4, but only if the atom pair at sites 2 and 4 is not in the state  $|\downarrow_2\downarrow_4\rangle$ . The gate  $C_{5,6}^{-(\uparrow,\downarrow)} T_{5,6}^\downarrow$  is applied next. This enables tunneling of the  $|\downarrow\rangle$  ( $\downarrow$ ) state from site 6 to site 5, conditioned on the pair of atoms at those sites not being in the configuration  $|\uparrow_5\downarrow_6\rangle$ . As a result, this operation modifies sites 5 as the output state of the target qubit, enabling completion of state transformation required for the CNOT operation, i.e.  $|q_c^{(1)} q_t^{(5)}\rangle = \text{CNOT} |q_c^{(1)} q_t^{(4)}\rangle$ . After the operation has been performed, atoms located at auxiliary sites 0, 2, 3, 4 and 6 are no longer needed and are discarded similarly to the disentangling operation for the  $X$  protocol.

## C. Error Mechanisms

To maintain a strong noise bias during quantum operations, replacement-type gates are designed to predominantly conserve the nature of the dominant error channels. However, achieving robust suppression of undesired error processes also requires careful qubit engineering at the hardware level. In this work, we addressed this by utilizing stretched nuclear spin states of neutral atom qubits with a large nuclear spin. Specifically, the qubit states are chosen to reside at the extreme ends of the magnetic quantum number spectrum in the ground-state manifold. Due to angular momentum selection rules, this configuration inherently forbids direct transitions between the two qubit states, providing intrinsic protection against unwanted couplings.

This advantageous property can extend to the metastable and Rydberg manifolds as well. In the metastable manifold, where atoms are temporarily ex-

cited for transport, only one of the qubit states is mainly affected due to the state-selective nature of the process. Consequently, imperfections in transport tend to primarily impact a single computational basis state, which can help maintain noise asymmetry. Similarly, in the Rydberg manifold, used for implementing entangling gates, spontaneous emission events are constrained by selection rules to decay within the same stretched subspace (i.e., conserving the sign of  $M_I$ ). This can lead to a preferential preservation of the original error bias, even in the presence of decoherence mechanisms such as photon scattering.

However, not all operations necessarily preserve this asymmetry. For instance, imperfections in the pick-and-drop process during storage-to-transport conversion, or phase errors in the entangling components of conditional tunneling gates, can introduce unwanted couplings between candidate qubits, ultimately leading to bias-breaking errors. Mitigating such effects requires these operations to be implemented with high fidelity. Although the system exhibits characteristics that are supportive of bias-preserving protocols, this compatibility is not absolute and depends critically on specific implementation details, which lie beyond the scope of this work.

On top of Pauli errors, the leakage error in neutral-atom platforms could substantially degrade the performance of quantum computational tasks, even if it is not dominant. This error could originate from atom loss or any leakage out of the computational subspace. Here, we outline several mitigation techniques that have been verified in experiments. In particular, state-selective imaging is a well-established technique that can be used to infer atom loss and leakage [110, 111]. In this approach, by leveraging the internal structure of the atom, both qubit states undergo independent imaging, hence detecting the leftover population out of the computational subspace, which in turn can be used to discard faulty simulation runs. Additionally, such measurements with single-site resolution allow for detecting the location of the leakage error, also known as leakage-to-erasure conversion [112, 113]. This enhances the gate performance conditioned on applying erasure checks at each step of our gate protocols. Note that the erasure conversion can also be done at a circuit level by transferring information about whether the qubit is present onto an auxiliary atom, e.g. see [114].

## V. CONCLUSION

In this work, we introduced the paradigm of replacement-type gates, which are designed for manipulating the qubit state in an extended Hilbert space instead of Bloch sphere rotations, therefore facilitating approximate noise bias preservation. Replacement-type gates are an option for qubits encoded in the internal states of quantum particles and rely on conditionally replacing the input particles with a superposition of can-

didate particles at an output site. We discussed the abstract concept of the two constituents of a replacement-type gate: a rearrangement operation which entangles the state of the input qubits with the configuration of a register of mobile candidate qubits, and a disentangling operation, which discards the original input qubits and all candidate qubits not in dedicated output sites by appropriate measurements.

As a concrete example, we presented protocols for replacement-type gates for Loss–DiVincenzo spin qubits, built from simple primitives which are either experimentally demonstrated or close to available techniques. Through a numerical evaluation we confirm the validity of the rearrangement operation, we find that the gates are strongly noise biased towards phase errors, and we identify the remaining sources of bit errors. The fidelity estimated with typical experimental parameters is lower than for comparable conventional gates, but our promising results warrant future theoretical or experimental studies aiming to find the optimal range of microscopic parameters, such as the magnetic gradient, or to optimize the shape of the detuning ramps.

To demonstrate the versatility of the replacement-type gate paradigm, we also develop an example realization for neutral atom qubits in optical tweezers. The discussion of the error sources suggests that a strong noise bias can be expected in this case as well, although some of the required operations here are currently hypothetical and no experimental reference is available. The formulation of an accurate error model and the assessment of gate fidelity and noise bias should be addressed in further research.

An open topic for future research is the development of protocols for other hardware platforms. Possible candidates that could support replacement-type gates are trapped ions, floating electrons on cryogenic substrates [115, 116], or molecular tweezer arrays [117–119]. Additional degrees of freedom of trapped atoms [120] or the vibration and rotation of a trapped molecule may allow for additional flexibility or may reduce the overhead. Another beneficial research direction is the design of chip layouts and blueprints that are optimized to accommodate the overhead of initializing and discarding auxiliary qubits within the limitations of specific hardware platforms.

As a next step towards exploiting the noise bias of the replacement-type gate for QEC, future research needs to balance the overhead required for approximately noise-bias-preserving replacement-type gates with the overhead for QEC. Special attention should be paid to the small but non-vanishing probability of charge errors, which may need tailored QEC codes [114, 121]. Finally, future research should investigate the interplay of repeated qubit replacement with time-correlated noise, such as  $1/f$  charge noise, and the consequences for QEC.

## ACKNOWLEDGMENTS

We thank Anette Messinger, Michael Schuler, Federico Dominguez, Philipp Aumann, Frederik Lohof and Christophe Goeller for helpful discussions. This study was supported by the Austrian Research Promotion Agency (FFG Project No. FO999909249, FFG Basisprogramm) as well as funded in part by the Austrian Research Promotion Agency (FFG Project No. 884444, QFTE 2020), NextGenerationEU via FFG and Quantum Austria (FFG Project No. FO999896208) and the Horizon Europe programme HORIZON- CL4-

2022-QUANTUM-02-SGA via the project 101113690 (PASQuanS2.1). Moreover, this publication has received funding by the Austrian Science Fund (FWF) SFB BeyondC Project No. F7108-N38, as well as funding within the QuantERA II Programme that is supported by the European Union's Horizon 2020 research and innovation programme under Grant Agreement No. 101017733. For the purpose of open access, the authors have applied a CC BY public copyright license to any Author Accepted Manuscript version arising from this submission. Furthermore, funding is acknowledged by the German Federal Ministry for Education and Research within ATIQ (Project No. 13N16127) and MuniQC-Atoms (Project No. 13N16080).

---

[1] J. Preskill, Quantum Computing in the NISQ era and beyond, *Quantum* **2**, 79 (2018).

[2] M. A. Nielsen and I. L. Chuang, *Quantum Computation and Quantum Information* (Cambridge University Press, Cambridge, 2000).

[3] J. Preskill, Reliable quantum computers, *Proc. R. Soc. Lond. A.* **454**, 385 (1998).

[4] P. W. Shor, Scheme for reducing decoherence in quantum computer memory, *Phys. Rev. A* **52**, R2493 (1995).

[5] A. R. Calderbank and P. W. Shor, Good quantum error-correcting codes exist, *Phys. Rev. A* **54**, 1098 (1996).

[6] A. M. Steane, Error correcting codes in quantum theory, *Phys. Rev. Lett.* **77**, 793 (1996).

[7] A. Kitaev, Fault-tolerant quantum computation by anyons, *Ann. Phys.* **303**, 2 (2003).

[8] A. G. Fowler, M. Mariantoni, J. M. Martinis, and A. N. Cleland, Surface codes: Towards practical large-scale quantum computation, *Phys. Rev. A* **86**, 032324 (2012).

[9] S. Bravyi, A. W. Cross, J. M. Gambetta, D. Maslov, P. Rall, and T. J. Yoder, High-threshold and low-overhead fault-tolerant quantum memory, *Nature* **627**, 778 (2024).

[10] A. Jayashankar and P. Mandayam, *Quantum error correction: Noise-adapted techniques and applications* (2024), arXiv:2208.00365 [quant-ph].

[11] S. Wu, T. A. Brun, and D. A. Lidar, *Bias-tailored single-shot quantum ldpc codes* (2025), arXiv:2507.02239 [quant-ph].

[12] K. Sahay, J. Jin, J. Claes, J. D. Thompson, and S. Puri, High-threshold codes for neutral-atom qubits with biased erasure errors, *Phys. Rev. X* **13**, 041013 (2023).

[13] B. Hetényi and J. R. Wootton, Tailoring quantum error correction to spin qubits, *Phys. Rev. A* **109**, 032433 (2024).

[14] J. Guillaud and M. Mirrahimi, Repetition cat qubits for fault-tolerant quantum computation, *Phys. Rev. X* **9**, 041053 (2019).

[15] C. Chamberland, K. Noh, P. Arrangoiz-Arriola, E. T. Campbell, C. T. Hann, J. Iverson, H. Puterman, T. C. Bohdanowicz, S. T. Flammia, A. Keller, G. Refael, J. Preskill, L. Jiang, A. H. Safavi-Naeini, O. Painter, and F. G. Brandão, Building a fault-tolerant quantum computer using concatenated cat codes, *PRX Quantum* **3**, 010329 (2022).

[16] D. Ruiz, J. Guillaud, A. Leverrier, M. Mirrahimi, and C. Vuillot, Ldpc-cat codes for low-overhead quantum computing in 2d, *Nature Communications* **16**, 1040 (2025).

[17] H. Puterman, K. Noh, C. T. Hann, G. S. MacCabe, S. Aghaeimeibodi, R. N. Patel, M. Lee, W. M. Jones, H. Moradinejad, R. Rodriguez, *et al.*, Hardware-efficient quantum error correction via concatenated bosonic qubits, *Nature* **638**, 927 (2025).

[18] I. Cong, H. Levine, A. Keesling, D. Bluvstein, S.-T. Wang, and M. D. Lukin, Hardware-efficient, fault-tolerant quantum computation with Rydberg atoms, *Phys. Rev. X* **12**, 021049 (2022).

[19] A. Messinger, V. Torggler, B. Klaver, M. Fellner, and W. Lechner, *Fault-tolerant quantum computing with the parity code and noise-biased qubits* (2024), arXiv:2404.11332 [quant-ph].

[20] G. Burkard, T. D. Ladd, A. Pan, J. M. Nichol, and J. R. Petta, Semiconductor spin qubits, *Rev. Mod. Phys.* **95**, 025003 (2023).

[21] R. Hanson, L. P. Kouwenhoven, J. R. Petta, S. Tarucha, and L. M. K. Vandersypen, Spins in few-electron quantum dots, *Rev. Mod. Phys.* **79**, 1217 (2007).

[22] F. Ye, A. Ellaboudy, D. Albrecht, R. Vudatha, N. T. Jacobson, and J. M. Nichol, Characterization of individual charge fluctuators in Si/SiGe quantum dots, *Phys. Rev. B* **110**, 235305 (2024).

[23] E. J. Connors, J. Nelson, L. F. Edge, and J. M. Nichol, Charge-noise spectroscopy of si/sige quantum dots via dynamically-decoupled exchange oscillations, *Nat. Commun.* **13**, 940 (2022).

[24] E. J. Connors, J. Nelson, H. Qiao, L. F. Edge, and J. M. Nichol, Low-frequency charge noise in Si/SiGe quantum dots, *Phys. Rev. B* **100**, 165305 (2019).

[25] J. S. Rojas-Arias, Y. Kojima, K. Takeda, T. N. Peter Stano, J. Yoneda, A. Noiri, T. Kobayashi, D. Loss, and S. Tarucha, *Spatial noise correlations beyond nearest-neighbor in <sup>28</sup>Si/SiGe spin qubits* (2023), arXiv:2302.11717 [cond-mat.mes-hall].

[26] L. Henriet, L. Beguin, A. Signoles, T. Lahaye, A. Browaeys, G.-O. Reymond, and C. Jurczak, Quantum computing with neutral atoms, *Quantum* **4**, 327 (2020).

[27] M. Morgado and S. Whitlock, Quantum simulation and

computing with Rydberg-interacting qubits, AVS Quantum Sci. **3**, 10.1116/5.0036562 (2021).

[28] Y. Matsumoto, M. D. Smet, L. Tryputen, S. L. de Snoo, S. V. Amitonov, A. Sammak, M. Rimbauch-Russ, G. Scappucci, and L. M. K. Vandersypen, Two-qubit logic and teleportation with mobile spin qubits in silicon (2025), arXiv:2503.15434 [quant-ph].

[29] A. R. Mills, C. R. Quinn, M. J. Gullans, A. J. Sigillito, M. M. Feldman, E. Nielsen, and J. R. Petta, Two-qubit silicon quantum processor with operation fidelity exceeding 99%, Sci. Adv. **8**, eabn5130 (2022).

[30] X. Xue, M. Russ, N. Samkharadze, B. Undseth, A. Sammak, G. Scappucci, and L. M. K. Vandersypen, Quantum logic with spin qubits crossing the surface code threshold, Nature **601**, 343 (2022).

[31] S. Jandura and G. Pupillo, Time-optimal two-and three-qubit gates for Rydberg atoms, Quantum **6**, 712 (2022).

[32] A. Pagano, S. Weber, D. Jaschke, T. Pfau, F. Meineert, S. Montangero, and H. P. Büchler, Error budgeting for a controlled-phase gate with strontium-88 Rydberg atoms, Phys. Rev. Res. **4**, 033019 (2022).

[33] C. D. Bruzewicz, J. Chiaverini, R. McConnell, and J. M. Sage, Trapped-ion quantum computing: Progress and challenges, Appl. Phys. Rev. **6**, 021314 (2019).

[34] S. A. Moses, C. H. Baldwin, M. S. Allman, R. Ancona, L. Ascarrunz, C. Barnes, J. Bartolotta, B. Bjork, P. Blanchard, M. Bohn, J. G. Bohnet, N. C. Brown, N. Q. Burdick, W. C. Burton, S. L. Campbell, J. P. Campora, C. Carron, J. Chambers, J. W. Chan, Y. H. Chen, A. Chernoguzov, E. Chertkov, J. Colina, J. P. Curtis, R. Daniel, M. DeCross, D. Deen, C. Delaney, J. M. Dreiling, C. T. Ertsgaard, J. Esposito, B. Estey, M. Fabrikant, C. Figgatt, C. Foltz, M. Foss-Feig, D. Francois, J. P. Gaebler, T. M. Gatterman, C. N. Gilbreth, J. Giles, E. Glynn, A. Hall, A. M. Hankin, A. Hansen, D. Hayes, B. Higashi, I. M. Hoffman, B. Horning, J. J. Hout, R. Jacobs, J. Johansen, L. Jones, J. Karcz, T. Klein, P. Lauria, P. Lee, D. Liefer, S. T. Lu, D. Lucchetti, C. Lytle, A. Malm, M. Matheny, B. Mathewson, K. Mayer, D. B. Miller, M. Mills, B. Neyenhuis, L. Nugent, S. Olson, J. Parks, G. N. Price, Z. Price, M. Pugh, A. Ransford, A. P. Reed, C. Roman, M. Rowe, C. Ryan-Anderson, S. Sanders, J. Sedlacek, P. Shevchuk, P. Siegfried, T. Skripka, B. Spaun, R. T. Sprenkle, R. P. Stutz, M. Swallows, R. I. Tobey, A. Tran, T. Tran, E. Vogt, C. Volin, J. Walker, A. M. Zolot, and J. M. Pino, A race-track trapped-ion quantum processor, Phys. Rev. X **13**, 041052 (2023).

[35] M. Mirrahimi, Z. Leghtas, V. V. Albert, S. Touzard, R. J. Schoelkopf, L. Jiang, and M. H. Devoret, Dynamically protected cat-qubits: a new paradigm for universal quantum computation, New Journal of Physics **16**, 045014 (2014).

[36] S. Puri, L. St-Jean, J. A. Gross, A. Grimm, N. E. Frattini, P. S. Iyer, A. Krishna, S. Touzard, L. Jiang, A. Blais, S. T. Flammia, and S. M. Girvin, Bias-preserving gates with stabilized cat qubits, Science advances **6**, eaay5901 (2020).

[37] J. M. Taylor, H. A. Engel, W. Dür, A. Yacoby, C. M. Marcus, P. Zoller, and M. D. Lukin, Fault-tolerant architecture for quantum computation using electrically controlled semiconductor spins, Nat. Phys. **1**, 177 (2005).

[38] A. Noiri, K. Takeda, T. Nakajima, T. Kobayashi, A. Sammak, G. Scappucci, and S. Tarucha, A shuttling-based two-qubit logic gate for linking distant silicon quantum processors, Nat. Commun. **13**, 5740 (2022).

[39] M. Künne, A. Willmes, M. Oberländer, C. Gorjaew, J. D. Teske, H. Bhardwaj, M. Beer, E. Kammerloher, R. Otten, I. Seidler, R. Xue, L. R. Schreiber, and H. Bluhm, The spibus architecture for scaling spin qubits with electron shuttling, Nat. Commun. **15**, 4977 (2024).

[40] F. Ginzel, M. Fellner, C. Ertler, L. R. Schreiber, H. Bluhm, and W. Lechner, Scalable parity architecture with a shuttling-based spin qubit processor, Phys. Rev. B **110**, 075302 (2024).

[41] M. Malinowski, D. Allcock, and C. Ballance, How to wire a 1000-qubit trapped-ion quantum computer, PRX Quantum **4**, 040313 (2023).

[42] B. Lekitsch, S. Weidt, A. G. Fowler, K. Mølmer, S. J. Devitt, C. Wunderlich, and W. K. Hensinger, Blueprint for a microwave trapped ion quantum computer, Sci. Adv. **3**, e1601540 (2017), <https://www.science.org/doi/pdf/10.1126/sciadv.1601540>.

[43] S. Weidt, J. Randall, S. C. Webster, K. Lake, A. E. Webb, I. Cohen, T. Navickas, B. Lekitsch, A. Retzker, and W. K. Hensinger, Trapped-ion quantum logic with global radiation fields, Phys. Rev. Lett. **117**, 220501 (2016).

[44] D. Bluvstein, H. Levine, G. Semeghini, T. T. Wang, S. Ebadi, M. Kalinowski, A. Keesling, N. Maskara, H. Pichler, M. Greiner, *et al.*, A quantum processor based on coherent transport of entangled atom arrays, Nature **604**, 451 (2022).

[45] R. Finkelstein, R. B.-S. Tsai, X. Sun, P. Scholl, S. Dierekci, T. Gefen, J. Choi, A. L. Shaw, and M. Endres, Universal quantum operations and ancilla-based readout for tweezer clocks, Nature **634**, 321 (2024).

[46] D. Bluvstein, A. A. Geim, S. H. Li, S. J. Evered, J. P. B. Ataides, G. Baranes, A. Gu, T. Manovitz, M. Xu, M. Kalinowski, S. Majid, C. Kokail, N. Maskara, E. C. Trapp, L. M. Stewart, S. Hollerith, H. Zhou, M. J. Gullans, S. F. Yelin, M. Greiner, V. Vuletic, M. Cain, and M. D. Lukin, Architectural mechanisms of a universal fault-tolerant quantum computer (2025), arXiv:2506.20661 [quant-ph].

[47] D. Loss and D. P. DiVincenzo, Quantum computation with quantum dots, Phys. Rev. A **57**, 120 (1998).

[48] F. A. Zwanenburg, A. S. Dzurak, A. Morello, M. Y. Simmons, L. C. L. Hollenberg, G. Klimeck, S. Rogge, S. N. Coppersmith, and M. A. Eriksson, Silicon quantum electronics, Rev. Mod. Phys. **85**, 961 (2013).

[49] M. Pioro-Ladrière, T. Obata, Y. Tokura, Y. S. Shin, T. Kubo, K. Yoshida, T. Taniyama, and S. Tarucha, Electrically driven single-electron spin resonance in a slanting zeeman field, Nat. Phys. **4**, 776 (2008).

[50] V. N. Golovach, M. Borhani, and D. Loss, Electric-dipole-induced spin resonance in quantum dots, Phys. Rev. B **74**, 165319 (2006).

[51] F. H. L. Koppens, C. Buijzer, K. J. Tielrooij, I. T. Vink, K. C. Nowack, T. Meunier, L. P. Kouwenhoven, and L. M. K. Vandersypen, Driven coherent oscillations of a single electron spin in a quantum dot, Nature **442**, 766 (2006).

[52] J. R. Petta, A. C. Johnson, J. M. Taylor, E. A. Laird, A. Yacoby, M. D. Lukin, C. M. Marcus, M. P. Hanson, and A. C. Gossard, Coherent

manipulation of coupled electron spins in semiconductor quantum dots, *Science* **309**, 2180 (2005), <https://www.science.org/doi/pdf/10.1126/science.1116955>.

[53] C. Barthel, D. J. Reilly, C. M. Marcus, M. P. Hanson, and A. C. Gossard, Rapid single-shot measurement of a singlet-triplet qubit, *Phys. Rev. Lett.* **103**, 160503 (2009).

[54] F. Ginzel, A. R. Mills, J. R. Petta, and G. Burkard, Spin shuttling in a silicon double quantum dot, *Phys. Rev. B* **102**, 195418 (2020).

[55] V. Langrock, J. A. Krzywda, N. Focke, I. Seidler, L. R. Schreiber, and L. Cywiński, Blueprint of a scalable spin qubit shuttle device for coherent mid-range qubit transfer in disordered si/sige/sio<sub>2</sub>, *PRX Quantum* **4**, 020305 (2023).

[56] B. Buonacorsi, B. Shaw, and J. Baugh, Simulated coherent electron shuttling in silicon quantum dots, *Phys. Rev. B* **102**, 125406 (2020).

[57] C. J. van Diepen, T.-K. Hsiao, U. Mukhopadhyay, C. Reichl, W. Wegscheider, and L. M. K. Vandersypen, Electron cascade for distant spin readout, *Nat. Commun.* **12**, 77 (2021).

[58] I. Fattal, J. V. Damme, B. Raes, C. Godfrin, G. Jaliel, K. Chen, T. VanCaekenbergh, A. Loenders, S. Kubicek, S. Massar, Y. Canvel, J. Jussot, Y. Shimura, R. Loo, D. Wan, M. Mongillo, , and K. D. Greve, Radio frequency single electron transmission spectroscopy of a semiconductor Si/SiGe quantum dot (2025), [arXiv:2504.05016 \[cond-mat.mes-hall\]](https://arxiv.org/abs/2504.05016).

[59] E. J. Connors, J. Nelson, and J. M. Nichol, Rapid high-fidelity spin-state readout in Si/Si-Ge quantum dots via rf reflectometry, *Phys. Rev. Appl.* **13**, 024019 (2020).

[60] K. Takeda, J. Kamioka, T. Otsuka, J. Yoneda, T. Nakajima, M. R. Delbecq, S. Amaha, G. Allison, T. Kodera, S. Oda, and S. Tarucha, A fault-tolerant addressable spin qubit in a natural silicon quantum dot, *Sci. Adv.* **2**, e1600694 (2016), <https://www.science.org/doi/pdf/10.1126/sciadv.1600694>.

[61] J. I. Colless, A. C. Mahoney, J. M. Hornibrook, A. C. Doherty, H. Lu, A. C. Gossard, and D. J. Reilly, Dispersive readout of a few-electron double quantum dot with fast rf gate sensors, *Phys. Rev. Lett.* **110**, 046805 (2013).

[62] B. Undseth, O. Pietx-Casas, E. Raymenants, M. Mehmandoost, M. T. Mądzik, S. G. J. Philips, S. L. de Snoo, D. J. Michalak, S. V. Amitonov, L. Tryputen, B. P. Wuetz, V. Fezzi, D. D. Esposti, A. Sammak, G. Scappucci, and L. M. K. Vandersypen, Hotter is easier: Unexpected temperature dependence of spin qubit frequencies, *Phys. Rev. X* **13**, 041015 (2023).

[63] F. K. Unseld, B. Undseth, E. Raymenants, Y. Matsumoto, S. Karwal, O. Pietx-Casas, A. S. Ivlev, M. Meyer, A. Sammak, M. Veldhorst, G. Scappucci, and L. M. K. Vandersypen, Baseband control of single-electron silicon spin qubits in two dimensions (2024), [arXiv:2412.05171 \[cond-mat.mes-hall\]](https://arxiv.org/abs/2412.05171).

[64] T. Fujisawa, D. G. Austing, Y. Tokura, Y. Hirayama, and S. Tarucha, Allowed and forbidden transitions in artificial hydrogen and helium atoms, *Nature* **419**, 278 (2002).

[65] J. Danon and Y. V. Nazarov, Pauli spin blockade in the presence of strong spin-orbit coupling, *Phys. Rev. B* **80**, 041301 (2009).

[66] D. Culcer, L. Cywiński, Q. Li, X. Hu, and S. Das Sarma, Quantum dot spin qubits in silicon: Multivalley physics, *Phys. Rev. B* **82**, 155312 (2010).

[67] A. Pályi and G. Burkard, Spin-valley blockade in carbon nanotube double quantum dots, *Phys. Rev. B* **82**, 155424 (2010).

[68] A. Pályi and G. Burkard, Hyperfine-induced valley mixing and the spin-valley blockade in carbon-based quantum dots, *Phys. Rev. B* **80**, 201404 (2009).

[69] C. Wittig, The landau-zener formula, *J. Phys. Chem. B* **109**, 8428 (2005).

[70] N. V. Vitanov and B. M. Garraway, Landau-zener model: Effects of finite coupling duration, *Phys. Rev. A* **53**, 4288 (1996).

[71] J. A. Krzywda and L. Cywiński, Adiabatic electron charge transfer between two quantum dots in presence of 1/f noise, *Phys. Rev. B* **101**, 035303 (2020).

[72] J. A. Krzywda and L. Cywiński, Interplay of charge noise and coupling to phonons in adiabatic electron transfer between quantum dots, *Phys. Rev. B* **104**, 075439 (2021).

[73] I. L. Chuang and M. A. Nielsen, Prescription for experimental determination of the dynamics of a quantum black box, *J. Mod. Opt.* **44**, 2455 (1997).

[74] J. F. Poyatos, J. I. Cirac, and P. Zoller, Complete characterization of a quantum process: The two-bit quantum gate, *Phys. Rev. Lett.* **78**, 390 (1997).

[75] J. L. O'Brien, G. J. Pryde, A. Gilchrist, D. F. V. James, N. K. Langford, T. C. Ralph, and A. G. White, Quantum process tomography of a controlled-not gate, *Phys. Rev. Lett.* **93**, 080502 (2004).

[76] K. Takeda, A. Noiri, T. Nakajima, L. C. Camenzind, T. Kobayashi, A. Sammak, G. Scappucci, and S. Tarucha, Rapid single-shot parity spin readout in a silicon double quantum dot with fidelity exceeding 99%, *npj Quant. Inf.* **10**, 22 (2024).

[77] J. A. Krzywda and L. Cywiński, Decoherence of electron spin qubit during transfer between two semiconductor quantum dots at low magnetic fields, *Phys. Rev. B* **111**, 115305 (2025).

[78] A. Zwerver, S. Amitonov, S. de Snoo, M. Mądzik, M. Rimbach-Russ, A. Sammak, G. Scappucci, and L. Vandersypen, Shutting an electron spin through a silicon quantum dot array, *PRX Quantum* **4**, 030303 (2023).

[79] H. Ribeiro, G. Burkard, J. R. Petta, H. Lu, and A. C. Gossard, Coherent adiabatic spin control in the presence of charge noise using tailored pulses, *Phys. Rev. Lett.* **110**, 086804 (2013).

[80] D. Fernández-Fernández, Y. Ban, and G. Platero, Quantum control of hole spin qubits in double quantum dots, *Phys. Rev. Appl.* **18**, 054090 (2022).

[81] C. V. Meinersen, S. Bosco, and M. Rimbach-Russ, Quantum geometric protocols for fast high-fidelity adiabatic state transfer (2024), [arXiv:2409.03084 \[quant-ph\]](https://arxiv.org/abs/2409.03084).

[82] J. R. F. Lima and G. Burkard, Interface and electromagnetic effects in the valley splitting of si quantum dots, *Mater. quantum technol.* **3**, 025004 (2023).

[83] L. E. A. Stehouwer, M. P. Losert, M. Rigot, D. D. Esposti, S. Martí-Sánchez, M. Rimbach-Russ, J. Arbiol, M. Friesen, and G. Scappucci, Engineering Ge profiles in Si/SiGe heterostructures for increased valley splitting (2025), [arXiv:2505.22295 \[cond-mat.mes-hall\]](https://arxiv.org/abs/2505.22295).

[84] T. McJunkin, E. R. MacQuarrie, L. Tom, S. F. Neyens, J. P. Dodson, B. Thorgrimsson, J. Corrigan, H. E. Er-

can, D. E. Savage, M. G. Lagally, R. Joynt, S. N. Coppersmith, M. Friesen, and M. A. Eriksson, Valley splittings in Si/SiGe quantum dots with a germanium spike in the silicon well, *Phys. Rev. B* **104**, 085406 (2021).

[85] T. McJunkin, B. Harpt, Y. Feng, M. P. Losert, R. Rahaman, J. P. Dodson, M. A. Wolfe, D. E. Savage, M. G. Lagally, S. N. Coppersmith, M. Friesen, R. Joynt, and M. A. Eriksson, Sige quantum wells with oscillating ge concentrations for quantum dot qubits, *Nat. Commun.* **13**, 7777 (2022).

[86] Y. Feng and R. Joynt, Enhanced valley splitting in Si layers with oscillatory Ge concentration, *Phys. Rev. B* **106**, 085304 (2022).

[87] B. Paquelet Wuetz, M. P. Losert, S. Koelling, L. E. A. Stehouwer, A.-M. J. Zwerver, S. G. J. Philips, M. T. Mađzik, X. Xue, G. Zheng, M. Lodari, S. V. Amitonov, N. Samkharadze, A. Sammak, L. M. K. Vandersypen, R. Rahman, S. N. Coppersmith, O. Moutanabbir, M. Friesen, and G. Scappucci, Atomic fluctuations lifting the energy degeneracy in Si/SiGe quantum dots, *Nat. Commun.* **13**, 7730 (2022).

[88] B. Paquelet Wuetz, D. Degli Esposti, A.-M. J. Zwerver, S. V. Amitonov, M. Botifoll, J. Arbiol, A. Sammak, L. M. K. Vandersypen, M. Russ, and G. Scappucci, Reducing charge noise in quantum dots by using thin silicon quantum wells, *Nat. Commun.* **14**, 1385 (2023).

[89] Y. Choi, J. M. Nichol, and E. Barnes, *Ballast charges for semiconductor spin qubits* (2024), arXiv:2405.14027 [cond-mat.mes-hall].

[90] A. J. Daley, Quantum computing and quantum simulation with group-II atoms, *Quant. Inf. Process* **10**, 865 (2011).

[91] A. Cooper, J. P. Covey, I. S. Madjarov, S. G. Porsev, M. S. Safronova, and M. Endres, Alkaline-earth atoms in optical tweezers, *Phys. Rev. X* **8**, 041055 (2018).

[92] A. Jenkins, J. W. Lis, A. Senoo, W. F. McGrew, and A. M. Kaufman, Ytterbium nuclear-spin qubits in an optical tweezer array, *Phys. Rev. X* **12**, 021027 (2022).

[93] S. Ma, A. P. Burgers, G. Liu, J. Wilson, B. Zhang, and J. D. Thompson, Universal gate operations on nuclear spin qubits in an optical tweezer array of  $^{171}\text{Yb}$  atoms, *Phys. Rev. X* **12**, 021028 (2022).

[94] J. W. Lis, A. Senoo, W. F. McGrew, F. Rönchen, A. Jenkins, and A. M. Kaufman, Midcircuit operations using the omg architecture in neutral atom arrays, *Phys. Rev. X* **13**, 041035 (2023).

[95] D. González-Cuadra, T. V. Zache, J. Carrasco, B. Kraus, and P. Zoller, Hardware efficient quantum simulation of non-abelian gauge theories with qudits on rydberg platforms, *Phys. Rev. Lett.* **129**, 160501 (2022).

[96] T. V. Zache, D. González-Cuadra, and P. Zoller, Fermion-qudit quantum processors for simulating lattice gauge theories with matter, *Quantum* **7**, 1140 (2023).

[97] R. Grimm, M. Weidemüller, and Y. B. Ovchinnikov, Optical dipole traps for neutral atoms (Academic Press, 2000) pp. 95–170.

[98] M. S. Safronova, Z. Zuhrianda, U. I. Safronova, and C. W. Clark, Extracting transition rates from zero-polarizability spectroscopy, *Phys. Rev. A* **92**, 040501 (2015).

[99] A. Heinz, A. J. Park, N. Šantić, J. Trautmann, S. G. Porsev, M. S. Safronova, I. Bloch, and S. Blatt, State-dependent optical lattices for the strontium optical qubit, *Phys. Rev. Lett.* **124**, 203201 (2020).

[100] G. Pagano, F. Scazza, and M. Foss-Feig, Fast and scalable quantum information processing with two-electron atoms in optical tweezer arrays, *Adv. Quant Technol.* **2**, 1800067 (2019).

[101] D. González-Cuadra, D. Bluvstein, M. Kalinowski, R. Kaubruegger, N. Maskara, P. Naldesi, T. V. Zache, A. M. Kaufman, M. D. Lukin, H. Pichler, B. Vermersch, J. Ye, and P. Zoller, Fermionic quantum processing with programmable neutral atom arrays, *Proc. Natl. Acad. Sci.* **120**, e2304294120 (2023).

[102] A. Pagano, D. Jaschke, W. Weiss, and S. Montangero, Optimal control transport of neutral atoms in optical tweezers at finite temperature, *Phys. Rev. Res.* **6**, 033282 (2024).

[103] S. Hwang, H. Hwang, K. Kim, A. Byun, K. Kim, S. Jeong, M. P. Soegianto, and J. Ahn, Fast and reliable atom transport by optical tweezers, *Opt. quantum* **3**, 64 (2025).

[104] S. J. Evered, D. Bluvstein, M. Kalinowski, S. Ebadi, T. Manovitz, H. Zhou, S. H. Li, A. A. Geim, T. T. Wang, N. Maskara, *et al.*, High-fidelity parallel entangling gates on a neutral-atom quantum computer, *Nature* **622**, 268 (2023).

[105] A. Cao, W. J. Eckner, T. Lukin Yelin, A. W. Young, S. Jandura, L. Yan, K. Kim, G. Pupillo, J. Ye, N. Darkwah Oppong, *et al.*, Multi-qubit gates and schrödinger cat states in an optical clock, *Nature* **634**, 315 (2024).

[106] J. Kazemi, M. Schuler, C. Ertler, and W. Lechner, *Multi-qubit parity gates for Rydberg atoms in various configurations* (2025), arXiv:2506.09686 [quant-ph].

[107] V. Sharma and E. J. Mueller, Driven-dissipative control of cold atoms in tilted optical lattices, *Phys. Rev. A* **103**, 043322 (2021).

[108] A. Schuckert, E. Crane, A. V. Gorshkov, M. Hafezi, and M. J. Gullans, *Fermion-qubit fault-tolerant quantum computing* (2024), arXiv:2411.08955 [quant-ph].

[109] A. L. Shaw, P. Scholl, R. Finkelstein, R. B.-S. Tsai, J. Choi, and M. Endres, Erasure cooling, control, and hyperentanglement of motion in optical tweezers, *Science* **388**, 845 (2025).

[110] T.-Y. Wu, A. Kumar, F. Giraldo, and D. S. Weiss, Stern–gerlach detection of neutral-atom qubits in a state-dependent optical lattice, *Nat. Phys.* **15**, 538 (2019).

[111] M. A. Norcia, W. B. Cairncross, K. Barnes, P. Battaglino, A. Brown, M. O. Brown, K. Cassella, C.-A. Chen, R. Coxe, D. Crow, J. Epstein, C. Griger, A. M. W. Jones, H. Kim, J. M. Kindem, J. King, S. S. Kondov, K. Kotru, J. Lauigan, M. Li, M. Lu, E. Megidish, J. Marjanovic, M. McDonald, T. Mittiga, J. A. Muniz, S. Narayanaswami, C. Nishiguchi, R. Notermans, T. Paule, K. A. Pawlak, L. S. Peng, A. Ryou, A. Smull, D. Stack, M. Stone, A. Sucich, M. Urbanek, R. J. M. van de Veerdonk, Z. Vendeiro, T. Wilkason, T.-Y. Wu, X. Xie, X. Zhang, and B. J. Bloom, Midcircuit qubit measurement and rearrangement in a  $^{171}\text{Yb}$  atomic array, *Phys. Rev. X* **13**, 041034 (2023).

[112] P. Scholl, A. L. Shaw, R. B.-S. Tsai, R. Finkelstein, J. Choi, and M. Endres, Erasure conversion in a high-fidelity Rydberg quantum simulator, *Nature* **622**, 273 (2023).

[113] S. Ma, G. Liu, P. Peng, B. Zhang, S. Jandura, J. Claes, A. P. Burgers, G. Pupillo, S. Puri, and J. D. Thompson,

High-fidelity gates and mid-circuit erasure conversion in an atomic qubit, [Nature 622, 279 \(2023\)](#).

[114] M. N. H. Chow, V. Buchemmarvari, S. Omanakuttan, B. J. Little, S. Pandey, I. H. Deutsch, and Y.-Y. Jau, Circuit-based leakage-to-erasure conversion in a neutral-atom quantum processor, [PRX Quantum 5, 040343 \(2024\)](#).

[115] E. Kawakami, J. Chen, M. Benito, and D. Konstantinov, Blueprint for quantum computing using electrons on helium, [Phys. Rev. Appl. 20, 054022 \(2023\)](#).

[116] A. Jennings, X. Zhou, I. Grytsenko, and E. Kawakami, Quantum computing using floating electrons on cryogenic substrates: Potential and challenges, [Appl. Phys. Lett. 124, 120501 \(2024\)](#).

[117] W. B. Cairncross, J. T. Zhang, L. R. B. Picard, Y. Yu, K. Wang, and K.-K. Ni, Assembly of a rovibrational ground state molecule in an optical tweezer, [Phys. Rev. Lett. 126, 123402 \(2021\)](#).

[118] C. M. Holland, Y. Lu, and L. W. Cheuk, On-demand entanglement of molecules in a reconfigurable optical tweezer array, [Science 382, 1143 \(2023\)](#).

[119] T. Langen, G. Valtolina, D. Wang, and J. Ye, Quantum state manipulation and cooling of ultracold molecules, [Nature Physics 20, 702 \(2024\)](#).

[120] W. Huie, C. Conefrey-Shinozaki, Z. Jia, P. Draper, , and J. P. Covey, Three-qubit encoding in ytterbium-171 atoms for simulating 1+1D QCD (2025), [arXiv:2507.18426 \[quant-ph\]](#).

[121] R. Stricker, D. Vodola, A. Erhard, L. Postler, M. Meth, M. Ringbauer, P. Schindler, T. Monz, M. Müller, and R. Blatt, Experimental deterministic correction of qubit loss, [Nature 585, 207 \(2020\)](#).